Title
A Compact, Ultrastable, Operando X-ray Ptychography Microscope at the Advanced Light Source

Author
Nowrouzi, Kasra

Publication Date
2019

Peer reviewed|Thesis/dissertation

A Compact, Ultrastable, Operando X-ray Ptychography Microscope at the Advanced Light Source

by

Kasra Nowrouzi

A dissertation submitted in partial satisfaction of the

requirements for the degree of

Doctor of Philosophy

in

Applied Science and Technology

in the

Graduate Division

of the

University of California, Berkeley

Committee in charge:

Professor Roger Falcone, Chair
Professor David Attwood
Professor Andrew Minor
Dr. David Shapiro
Professor Laura Waller

Summer 2019

A Compact, Ultrastable, Operando X-ray Ptychography Microscope at the Advanced Light Source

Abstract

A Compact, Ultrastable, Operando X-ray Ptychography Microscope at the Advanced Light Source

by

Kasra Nowrouzi

Doctor of Philosophy in Applied Science and Technology

University of California, Berkeley

Professor Roger Falcone, Chair

X-ray imaging traces its roots back to the discovery of x-rays by Röntgen in 1901, in the form of simple projection imaging. Several decades later, fabrication of x-ray optics enabled image formation at higher resolutions, leading to microscopy. Nevertheless, microscopy at resolutions on the order of the x-ray wavelength has only become possible in recent years, after a host of enabling technologies, including high-brightness coherent sources, advanced detectors, high-performance computers and algorithms, and precision instrumentation were brought together by multidisciplinary teams of scientists to form one coherent imaging system. Today, x-ray ptychography microscopes operating at modern synchrotron facilities can image thick samples at unprecedented resolutions, and yield chemical information about the sample, enabling novel material science studies. The field is rapidly developing, and the advent of new Diffraction Limited Storage Ring (DLSR) sources around the world promises to provide new opportunities with increased coherent brightness.

This dissertation presents new advances in instrumentation and analysis at the Advanced Light Source at Lawrence Berkeley National Lab. A new x-ray ptychography microscope is described, compact in size and ultrastable in both vibrations and drift, enabling better than 3nm spatial resolution, and integrating a TEM-compatible in-situ sample holder to enable multimodal, operando, and cryogenic experiments. A new approach to the analysis of spectro-microscopic data is presented, combining low-resolution STXM and high-resolution ptychography images to produce chemical maps at high resolution without a priori reference spectra. This is achieved by collecting STXM data at fine x-ray energy increments, from which spectra are extracted by PCA and clustering. The ptychography data, collected at only a few energies, is then fitted to these extracted spectra. Finally, new ideas are explored to speed up scanning in ptychography, leading to a reduction in scan overhead, dose, and data collection times. This is done in two ways: firstly, a simple, yet effective, scanning algorithm is introduced to adjust feedback parameters for the piezo stage scanning the zone plate, reducing the scan overhead time. Secondly, lower density scan patterns and their effects on quality and resolution of reconstructions are investigated; based on these, ideas

are proposed to intelligently reduce the total number of diffraction patterns collected, while only minimally affecting results. Combined with the promise of increased coherent flux with upcoming DLSRs, leading to much shorter exposure times, these speedups will enable much faster ptychography scans, greatly facilitating tomography or in-situ experiments, currently taking many hours or days.

To The Fire, Within and Without,
Burning Proud,
Giving Rise to Generative Chaos,
And Evolved Order

To Those Who Shared the Trek,
Shared in The Fire,
And Burned Along,
As We Grew Older

K.N., 2019

Contents

List of Figures

Acknowledgments

I consider myself very lucky to have benefited from a very diverse atmosphere during my PhD years at UC Berkeley and the Advanced Light Source at Lawrence Berkeley National Lab, surrounded by researchers from a vast range of personal and scientific backgrounds, working on many fun and challenging problems within multidisciplinary teams. I would like to thank my advisor, Professor Roger Falcone, for guiding me through these years. Despite always having had a wide range of important responsibilities to attend to, Roger was always accessible and very generous with his valuable time and insightful advice.

I would like to thank my supervisor, Dr. David Shapiro, who oversaw my research activities within the Microscopy group at the ALS. Ever since I joined the ALS in 2014, David trusted me with many opportunities to work on different projects, and encouraged me to explore and take risks, which I very much enjoyed and appreciated, as my PhD research slowly began to take shape. I would like to thank the Microscopy group, led by David; I learned a lot from this group. Matthew Marcus, Hendrik Ohldag, and Young-Sang Yu were all very generous with their time and advice, on which I depended countless times through the years. Richard Celestre taught me a lot in a range of topics as we worked together on the Nanosurveyor 2 project. Instrumentation projects can become very frustrating at times; I am thankful to David and Rich for helping to the challenge a pleasant, collaborative undertaking. Last but not least, I am thankful to Drs. Bjoern Enders, Jungjin Park, and Sam Kalirai, the postdocs in our group, from whom I learned a lot and with whom I spent many hours exchanging ideas, starting out as colleagues and becoming friends. Outside of the Microscopy group, I was also fortunate to learn from and work with other scientists and engineers at LBL. These included Dr. Stefano Marchesini, with whom I had a lot of stimulating discussions, Lee Yang, with whom I collaborated on the electrical systems of Nanosurveyor 2, and Dr. Antoine Wojdyla, whose collaborative spirit across disciplines is always inspiring.

None of my work at ALS would have been possible if not for Dr. Howard Padmore, who interviewed me and gave me the opportunity to work here in the first place. I am grateful for this and the opportunities that followed. I would like to thank the taxpayers and the United States Department of Energy for supporting my research through my employment at LBL during my PhD. This research used resources of the Advanced Light Source, which is a DOE Office of Science User Facility, under contract no. DE-AC02-05CH11231. This work was supported by STROBE: A National Science Foundation Science & Technology Center (DMR-1548924). I would like to thank NSF and STROBE for bringing researchers from various research institutions together, and facilitating and supporting collaboration to further the science of imaging.

Aside from working 'up the hill' at LBL, I also spent time on campus at UC Berkeley, where I took classes and learned from many fantastic professors. I would like to thank Professor Andrew Minor, from whom I learned about electron microscopy, and Professor Laura Waller, from whom I learned about imaging and statistical signal processing, and who

also welcomed me into her group meetings. It was always truly a pleasure to interact with Andy and Laura, and with their research groups.

Within UC Berkeley, I was a student in the Applied Science and Technology graduate group (AS&T), a unique interdisciplinary program with a small but impressive student body from all backgrounds. I found it inspiring from the very beginning to see how the students work together to create a cohesive culture, despite being dispersed across multiple home departments. I benefited from this atmosphere even before officially entering the program: I would like to thank Brian Shaw for introducing me to the program and guiding me through the process as I got in and settled in as a student. It was my honor and privilege to later get to contribute to AS&T, representing it at the Graduate Assembly, and in the process becoming part of a great fellowship of upstanding individuals. As I depart, it gives me pride and hope to see the AS&T community thriving more than ever; and I'm confident the future is bright with the leadership of our current students, including Carlos Biaou, Liona Fan-Chiang, Madeleine Gordon, Akel Hashim, Fumika Isono, Emma Regan, and Colin Wahl.

Mentorship is a critical component of growth for any graduate student and any program, though it may be more difficult to find at larger research universities. The AS&T student community has been fortunate to benefit from the mentorship of Professor David Attwood. He has been the number one active advocate for the students, keeping their best interests at heart, and sets the example for other students and faculty to follow. Though his reputation and involvement dates farther back than the institutional memory of the current student body, we all have either directly benefited from his advocacy and mentorship, or know someone who has. I personally feel very fortunate and honored to count him as my mentor.

During my PhD years, I found it very important to establish balanced routines and live a balanced life. The practice of karate became a significant part of this, and a source of focus, health, and fellowship. I would like to thank Sensei Hidetaka Abe for leading the UC Berkeley Karate Club with great spirit, and making it a safe, supportive, and convivial atmosphere. I would also like to thank Eugene Malikin, Laura Lowman, Itai Trilnick, Angel Ryono, Kirk Hewett, Dmytro Oliinychenko, Tohma Judge, Akito Kusaka, and others with whom I trained. I value and cherish the friendships we formed over the years.

Starting a PhD and doing well in it requires a lifetime of education and preparation. I would like to thank my family for my upbringing. I would like to thank my late father, Kamal, who managed to deeply shape my character in the short years he was with us. His incorruptible integrity, and his combination of sharp yet unassuming intelligence, quiet strength, and deep and genuine kindness towards all still inspire and guide me today. I would like to thank my mother, Farideh Fakouri, a true fighter who gave her family all her heart. I hope to one day become deserving of all her sacrifice. And I would like to thank my brother, Kayvan, one of the strongest, most responsible, most kindhearted people I know. I am lucky to have such a sparring partner for life. I would also like to thank Mona, my former partner, who encouraged and supported my decision to do a PhD in the years leading up to it, and who stood by me throughout the struggles of graduate school. Lastly, I would like to thank my uncle, Robert Fakuri, who, with his immigration to California more than four decades ago, paved the path for my family to follow.

Chapter 1

Introduction to X-ray Microscopy

This chapter starts by motivating x-rays as carriers of information in microscopy and reviewing x-ray interaction with matter. X-ray optics and coherence of the beam are discussed next, leading up to traditional full-field and scanning probe techniques. Finally, shortcomings of traditional techniques are used to motivate Coherent Diffractive Imaging, to be discussed in chapter 2. Throughout most of this introductory chapter, we closely follow chapters 1-4 and 10-11 of X-rays and Extreme Ultraviolet Radiation, by David Attwood and Anne Sakdinawat [1].

1.1 Background and Motivation

1.1.1 The X-ray as the Imaging Medium

X-ray imaging is intrinsically tied to the discovery of x-rays, leading to the inaugural Nobel prize in Physics, awarded in 1901 to Wilhelm Röntgen, after whom x-rays are named in the German language (Röntgenstrahlung; literally: "Röntgen radiation"). The type of imaging involved in this discovery was simple projection imaging: he placed various objects between a source of x-rays and a fluorescent screen (or a photographic plate), and observed the pattern formed, with no optical components involved [2]. Since then, we have understood this mysterious radiation to be just another interval within the Electromagnetic spectrum, as visualized in Fig. 1.1.

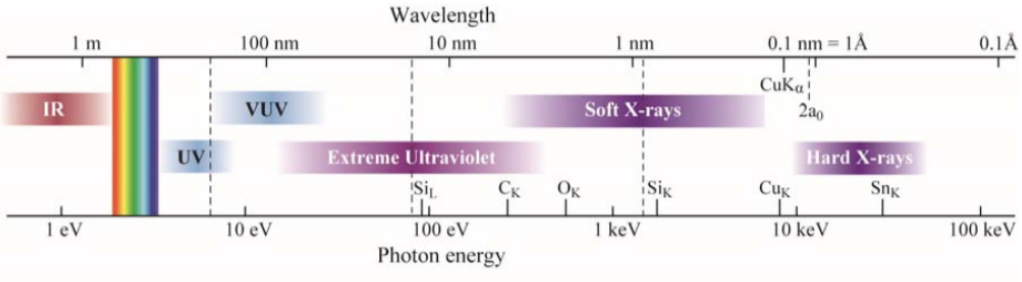

Figure 1.1: X-rays as a part of the Electromagnetic spectrum, displayed by both wavelength and photon energy (in eV). Reproduced from Attwood and Sakdinawat [1] with permission.

Today, more complicated modes of x-ray imaging have become commonplace. In this dissertation, we concern ourselves with microscopy as the imaging mode. In particular, in this section, we seek to give context to x-ray microscopy alongside visible light and electrons as two popular means of microscopy. (It should be noted that there are a range of other means available for microscopy, including, for example, neutrons [3] and helium ions [4].)

Why use x-rays at all alongside visible light and electron techniques?

Let's start with spatial resolution, a measure of the smallest features distinguishable by the microscope. One such measure, widely in use today, is the Rayleigh criterion, introduced by Lord Rayleigh [5]:

$$\Delta r_{Rayl.} = \frac{0.61\lambda}{NA} \tag{1.1}$$

where λ denotes the wavelength and $NA = n \sin\theta$ is the numerical aperture, with n the refractive index, and θ the largest scattering angle allowed through the imaging system. Although the refractive index and the scattering angle tend to work to the benefit of visible light (due to the weaker interaction of x-rays with matter, as we will see later in this chapter), the fact that x-ray wavelengths are orders of magnitude smaller than those of visible light establishes a fundamental resolution limit far in favor of x-rays. On the other hand, the de-Broglie wavelength of the electron beam in a typical electron microscope is still much smaller than x-ray wavelengths [6, page 112]; and electron microscopes do indeed achieve higher resolutions compared to all other techniques. But spatial resolution is not the only important figure of merit in microscopy.

Electrons and x-rays interact with matter in fundamentally different ways, giving rise to many practical consequences in microscopy. One such consequence is the difference between attenuation lengths of the two in a given sample: although the exact lengths vary, depending on the sample as well as the energies of the x-ray and electron beams, the attenuation lengths for x-rays tend to be substantially longer than for electrons, giving x-rays access to thicker samples [7].

Aside from making thicker samples accessible, x-ray techniques also "provide a wealth of information from elemental and chemical composition to molecular orientation and magnetic order in specimens, which often can not be measured by any other technique" [8, 9]. Together, these characteristics can enable new scientific applications, allowing, for example, detailed chemical maps (through oxidation state) of charge-discharge state of novel battery materials at nanometer scale resolutions [10].

In order to shed more light on the points above, we need to understand x-ray interaction with matter in more detail:

1.1.2 X-Ray Interaction with Matter

An x-ray beam can be described as a wave, with an amplitude and a phase associated with it at each point. When this wave enters the sample under study and interacts with it, both the amplitude and the phase could be modified by the interaction. Here, we attempt to build an intuition for this interaction and introduce the relevant formulas. For a full, rigorous derivation of all formulas in detail, the reader is referred to chapters 2 and 3 of [1], which we roughly follow here.

X-rays carry electromagnetic energy. As such, they interact with, and exert force on, charged particles, as described by the Lorentz force: $\mathbf{F} = q(\mathbf{E} + \mathbf{v} \times \mathbf{B})$. Although electrons and protons carry the same electric charge and would thus experience the same force in the same field, the electrons in an atom experience orders of magnitude stronger acceleration, since they are orders of magnitude less massive than protons. We thus focus on the interaction of electrons with the x-ray beam. We will do this by starting with a free electron, then extending to a bound electron and a collection of bound electrons in an atom, and finally considering a bulk of material made of atoms.

A free electron in the path of incident electromagnetic radiation experiences force (and thus acceleration) due to the oscillating EM field. The oscillating charge, in return, generates EM radiation. A full derivation reveals the instantaneous power emitted by such an oscillating electron with acceleration $\mathbf{a}$ observed at a distance r to be

$$\mathbf{S}(\mathbf{r}, t) = \frac{e^2 |\mathbf{a}|^2 \sin^2 \Theta}{16\pi^2 \epsilon_0 c^3 r^2} \mathbf{k_0} \tag{1.2}$$

where e is elementary charge and Θ is the angle between $\mathbf{a}$ and the direction of observation, $\mathbf{k_0}$. This angular dependence of radiated power indicates that when a plane wave (or parallel rays, in the ray picture) of x-rays is incident on an electron, the electron effectively redirects the radiation in all angles. We refer to this phenomenon as *scattering*, and with it associate a parameter σ called the *scattering cross-section*

$$\sigma \equiv \frac{\bar{P}_{scatt.}}{|\bar{\mathbf{S}}_i|} \tag{1.3}$$

where the numerator is the average scattered power, and the denominator is the average incident power per unit area (resulting in units of area for the scattering cross-section, as expected). For a free electron, this parameter turns out to be a constant

$$\sigma_e = \frac{8\pi}{3} r_e^2 \tag{1.4}$$

where r_e is the classical electron radius. (One way to classically think of this, with the classical cross-section area of the electron in the path of incident radiation being πr_e^2, is that a free electron scatters the radiation incident on roughly three times the area of its classical cross-section.)

In the case of a bound electron (as one bound to a positively charged nucleus of an atom) the derivation leading to the above result is complicated by the presence of the restoring force of the nucleus, with which a resonance frequency ω_s is associated. Accounting for this, and also including a dissipative parameter γ to account for the oscillator's energy loss (with the assumption $\gamma/\omega \ll 1$ where ω is the frequency of the incident radiation), the scattering cross-section for the bound electron becomes

$$\sigma = \frac{8\pi}{3} r_e^2 \frac{\omega^4}{\left(\omega^2 - \omega_s^2\right)^2 + \left(\gamma\omega\right)^2} \tag{1.5}$$

We note the strong frequency dependence of scattering cross-section for the bound electron. In particular, there is a strong amplification on resonance (where $\omega \simeq \omega_s$), while the result tends to the free electron case in the high frequency limit $\omega \gg \omega_s$. Although of little relevance to our x-ray context, the reader may find it of interest to note that the low-frequency limit of this cross-section describes Rayleigh scattering [11].

Equation 1.5 serves as the starting point for the calculation of a multi-electron atom's cross-section of scattering, where one needs to keep track of contributions by each bound electron. A schematic of this is visualized in Fig. 1.2:

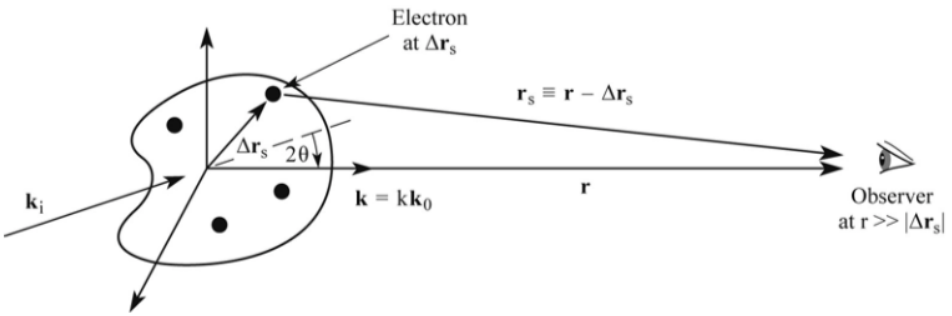

Figure 1.2: A multi-electron atom modeled as a collection of bound electrons around a nucleus of charge $+Ze$, viewed by an observer in the far-field. Reproduced from Attwood and Sakdinawat [1] with permission.

The scattering cross-section for the whole atom calculated in this way becomes still more complicated:

$$\sigma = \frac{8\pi}{3}|f|^2 r_e^2 \tag{1.6}$$

where

$$f(\Delta\mathbf{k}, \omega) = \sum_{s=1}^{Z} \frac{\omega^2 e^{-i\Delta\mathbf{k}\cdot\Delta\mathbf{r_s}}}{\omega^2 - \omega_s^2 + i\gamma\omega} \tag{1.7}$$

contains the frequency-dependent contributions of the ensemble of electrons, and is called the *atomic scattering factor*. This is a complex term and contains phase contributions due to relative placement of electrons within the atom. This term, in general, is non-trivial to calculate; but it does simplify in specific cases where $\Delta\mathbf{k}\cdot\Delta\mathbf{r_s} \to 0$. With parameters as defined in Fig. 1.2 and $k_i = 2\pi/\lambda$ being the wavevector of the incident wave, we have $|\Delta\mathbf{k}| = 2k_i \sin\theta = \frac{4\pi}{\lambda}\sin\theta$. Noting that the electron distribution in an atom is within a distance on the order of the Bohr radius a_0, we find the following bound:

$$|\Delta\mathbf{k}\cdot\Delta\mathbf{r_s}| \leq \frac{4\pi a_0}{\lambda}\sin\theta \tag{1.8}$$

and thus conclude that the left hand side will vanish in either of the following circumstances:

- forward scattering, where $\theta \ll 1$
- long wavelength limit, where $\lambda/a_0 \gg 1$

thus simplifying Equation 1.7

$$f^0(\omega) = \sum_s \frac{g_s\omega^2}{\omega^2 - \omega_s^2 + i\gamma\omega} \tag{1.9}$$

The parameter g_s here serves the purpose of accounting for multiple electrons, such as those in the same orbital, sharing the same resonance frequency ω_s, and is termed *oscillator strength*. It is then naturally subject to constraint $\sum_s g_s = Z$.

Note that with Bohr radius being of sub-Angstrom scale, the condition $\lambda/a_0 \gg 1$ is satisfied for a significant portion of the x-ray spectrum, where Equation 1.9 serves as a valid approximation. But, as a matter of more immediate practical importance, microscopy in general involves not just scattering from one multi-electron atom, but a collection of atoms scattering in concert. This collective behavior is captured by the complex *index of refraction*, which depends on forward scattering, as we will see shortly. Thus, we regard $f^0(\omega)$ as a valid approximation to $f(\omega)$ insofar as microscopy is concerned.

The derivation of the index of refraction starts with the wave equation for EM waves

$$\left(\frac{\partial^2}{\partial t^2} - c^2\nabla^2\right)\mathbf{E}(\mathbf{r},t) = \frac{-1}{\epsilon_0}\left[\frac{\partial \mathbf{J}(\mathbf{r},t)}{\partial t} + c^2\nabla\rho(\mathbf{r},t)\right] \tag{1.10}$$

which itself follows from Maxwell's equations [1, page 29]. After various substitutions and rearrangements [1, pages 61-63], we arrive at

$$\left[\left(1 - \frac{e^2 n_a}{\epsilon_0 m}\sum_s \frac{g_s}{(\omega^2 - \omega_s^2) + i\gamma\omega}\right)\frac{\partial^2}{\partial t^2} - c^2\nabla^2\right]\mathbf{E}_T(\mathbf{r},t) = 0 \tag{1.11}$$

which can be rewritten as

$$\left[\frac{\partial^2}{\partial t^2} - \frac{c^2}{n^2(\omega)}\nabla^2\right]\mathbf{E}_T(\mathbf{r},t) = 0 \tag{1.12}$$

with the index of refraction, $n(\omega)$, defined as

$$n(\omega) \equiv \left[1 - \frac{e^2 n_a}{\epsilon_0 m}\sum_s \frac{g_s}{(\omega^2 - \omega_s^2) + i\gamma\omega}\right]^{1/2} \tag{1.13}$$

as the parameter that modifies c, the phase velocity of light in vacuum. In the x-ray regime, due to the magnitude of ω, the deviation of $n(\omega)$ from unity is extremely small; and so Equation 1.13 can be written as

$$n(\omega) = 1 - \frac{e^2 n_a}{2\epsilon_0 m}\sum_s \frac{g_s}{(\omega^2 - \omega_s^2) + i\gamma\omega} \tag{1.14}$$

The summation term here reminds us of f^0 in Equation 1.9, off by $\omega^2 = (2\pi c/\lambda)^2$ where λ is the wavelength in vacuum. Decomposing f^0 into its real and imaginary parts

$$f^0(\omega) = f_1^0(\omega) + i f_2^0(\omega) \tag{1.15}$$

and noting the classical radius of the electron as $r_0 = e^2/4\pi\epsilon_0 mc^2$, we could rewrite 1.14 as

$$n(\omega) = 1 - \frac{n_a r_e \lambda^2}{2\pi}\left[f_1^0(\omega) - i f_2^0(\omega)\right] \tag{1.16}$$

It is customary to simplify notation by rewriting the above as

$$\boxed{n(\omega) = 1 - \delta + i\beta} \tag{1.17}$$

where

$$\boxed{\begin{aligned}\delta &= \frac{n_a r_e \lambda^2}{2\pi} f_1^0(\omega) \qquad (1.18a)\\ \beta &= \frac{n_a r_e \lambda^2}{2\pi} f_2^0(\omega) \qquad (1.18b)\end{aligned}}$$

The parameters δ and β, the real and imaginary parts of the deviation from unity of the refractive index, account for a material's effect on phase velocity and the amplitude of the x-ray wave compared to vacuum. In the x-ray regime, these parameters are quite small (typically orders of magnitude smaller than unity) and get even smaller with increasing x-ray energy (as expected, due to the λ^2 factor in 1.18 and also in the behavior of f^0.) An important general behavior of note is that although δ and β are of roughly the same order for x-ray energies around a keV, β experiences a much steeper decline with increasing energy compared to δ, resulting in a difference of several orders of magnitude by the time we are in the several keV range. (An example of this for silicon is plotted in Fig. 1.3.) This has practical implications in microscopy: techniques based on both absorption contrast and phase contrast mechanisms work well at lower energies, while microscopy at higher energies tends to rely on phase contrast for better results [12].

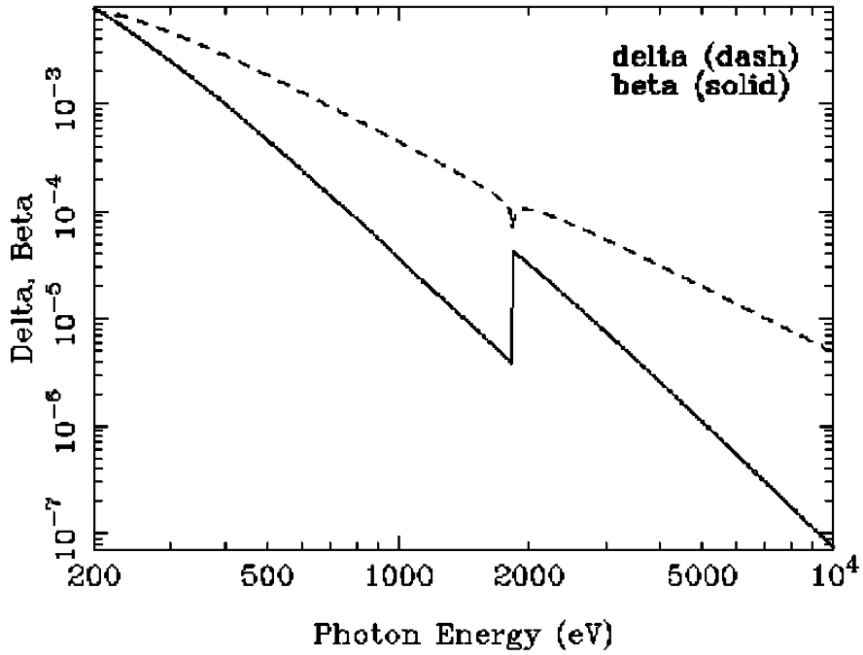

Figure 1.3: An example of delta/beta behavior over a range of soft and hard x-ray energies. From CXRO's x-ray database, http://henke.lbl.gov/optical_constants/getdb2.html

The dependence of δ and β on x-ray energy/wavelength (and the practical implications thereof) is significant enough that by convention the x-ray spectrum has been divided into roughly two main regimes: the *soft x-ray* regime for wavelengths on the order of a nanometer, and the *hard x-ray* regime for more energetic x-rays. Hard x-rays experience much less attenuation and phase shift compared to soft x-rays, and are thus more suitable for probing thicker samples. However, there is no abrupt physical reference for the threshold between the two regimes, and so the official convention for the cutoff varies by source, but is in the several

keV energy range. The transitory range between soft and hard x-rays is sometimes referred to as the *tender x-ray* regime. (For literature examples on various numbers delimiting soft, tender, and hard x-rays, see e.g. [13], [14], [15].)

To more clearly relate δ and β to phase velocity modification and amplitude attenuation, we can write down the expression for a plane wave in the standard form:

$$\mathbf{E}(\mathbf{r}, t) = \mathbf{E}_0 e^{-i(\omega t - \mathbf{k}\cdot\mathbf{r})} \tag{1.19}$$

Now, substituting 1.17 into the dispersion relation

$$\frac{\omega}{k} = \frac{c}{n} = \frac{c}{1 - \delta + i\beta} \tag{1.20}$$

we solve for k

$$k = \frac{\omega}{c}(1 - \delta + i\beta) \tag{1.21}$$

and substitute into 1.19 to obtain

$$\mathbf{E}(\mathbf{r}, t) = \mathbf{E}_0 e^{-i\omega(t - r/c)} e^{-i(2\pi\delta/\lambda)r} e^{-(2\pi\beta/\lambda)r} \tag{1.22}$$

where the first exponential describes vacuum propagation, the second describes the phase shift due to δ of the material, and the last exponential describes amplitude attenuation due to absorption in the material, related to β.

Following this form, we can immediately write down the phase shift in the material of thickness Δr as

$$\boxed{\Delta\phi = \frac{2\pi\delta}{\lambda}\Delta r} \tag{1.23}$$

To characterize the amplitude attenuation, we use the concept of *absorption length* (or *attenuation length*), denoted by l_{abs} and defined as the distance in the material where the intensity of the wave is reduced by a factor of e. This corresponds to an E-field reduction of $e^{1/2}$, since the intensity of the EM wave is proportional to the square of the amplitude of the electric field. We then have:

$$e^{-(2\pi\beta/\lambda)l_{abs}} = e^{-1/2} \tag{1.24}$$

Solving for the absorption length, we find

$$\boxed{l_{abs} = \frac{\lambda}{4\pi\beta}} \tag{1.25}$$

It should be noted that while x-rays do attenuate in matter due to absorption (as with other forms of radiation), the phase shift they experience (as denoted in Equation 1.23) tends to be positive, due to a positive (though very small) δ. This is because the phase velocity

of x-rays in matter is *higher* than in vacuum, leading to a phase advance, unlike most other parts of the EM spectrum. (It should be stressed that this is the phase velocity and not the group velocity of the EM wave.) Fig. 1.4 visualizes this point.

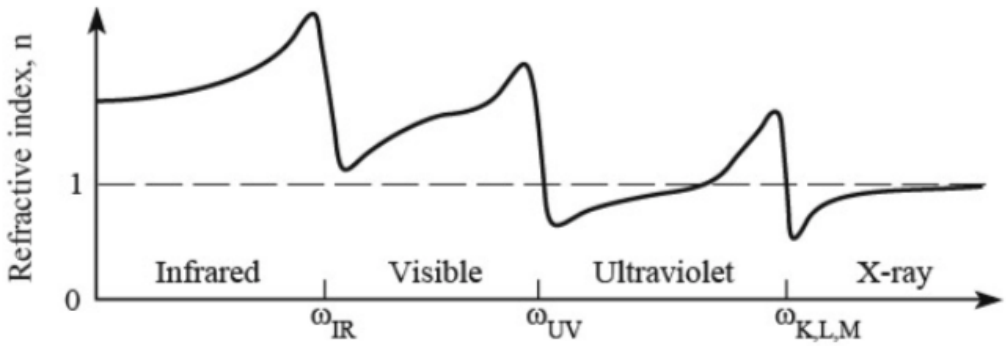

Figure 1.4: The general behavior of the real part of the index of refraction for various parts of the EM spectrum. Reproduced from Attwood and Sakdinawat [1] with permission.

To recap, electrons in a sample under study interact with the incident x-ray beam in concert to give rise to bulk effects, i.e. intensity attenuation and phase change, characterized by the complex index of refraction and dependent on sample thickness and x-ray wavelength. X-ray microscopy involves extracting as much of this information from the sample as desired and possible. As we will see, some traditional techniques only yield information about intensity attenuation through absorption, whereas newer techniques, such as ptychography, pertinent to this thesis, simultaneously quantify both absorption and phase change.

1.2 Considerations in X-Ray Imaging Modalities

As discussed in section 1.1.1, the discovery of x-rays was inextricably linked to x-ray imaging, of projection imaging modality. Since then, more advanced imaging modalities have been developed over the decades. In order to enable these developments, scientists and engineers have had to overcome several barriers, and invent and implement various technologies. Some of the challenges that have been addressed have involved creating better x-ray sources with suitable properties, fabricating x-ray optics, and increasing computational capabilities.

In this section and the next, we discuss some of these issues and relate them to various imaging modalities.

1.2.1 The X-Ray Spectrum and X-Ray Optics

A natural step in creating an imaging system has traditionally been the development of optics, used to focus beams and form images. Here we briefly mention some important

optics used in x-ray imaging.

As mentioned in 1.1.2, the parameters δ and β are orders of magnitude smaller than unity in the x-ray regime (indicating the weakness of interaction with matter), and they get much smaller with increasing x-ray energy. This makes x-ray optics development a much different enterprise compared to visible light, though there are still some similarities in at least one case: the *compound refractive lens* [16]. This is where we start.

In a visible light lens (take a convex lens, for example), the goal of bringing incident rays into focus is achieved by bending each ray in two places: the entry interface into the lens and the exit interface, where the rays leave the lens. The bending happens due to refraction (with which we assume the reader is familiar), and the lens surfaces are shaped to bring parallel incident rays into focus. A compound refractive lens (CRL) is very similar, with two main differences: 1) To achieve the same focusing effect, the placement of lens material and vacuum (or air) needs to be swapped. This is because in the case of x-rays, the index of refraction is higher in vacuum than in material, as discussed in 1.1.2, which inverts the bending direction at vacuum-material interface. 2) Due to the weakness of refraction at x-ray wavelengths (since the refractive index is close to unity), a single such structure has little focusing power. They are thus fabricated as a series in tandem (hence the term "compound".)

To find the focal length of a biconcave CRL, we start with the Lensmaker's Formula [17, p. 158]:

$$\frac{1}{f} = (n-1)\left(\frac{1}{R_1} - \frac{1}{R_2}\right) \tag{1.26}$$

and substitute $R \equiv R_2 = -R_1$ (for a biconcave lens) and $n = 1 - \delta$ (using only the real part of the refractive index, which accounts for the bending of rays) to find $f = R/2\delta$. This effect is amplified by the number N of total structures in series, to effectively yield:

$$f = \frac{R}{2N\delta} \tag{1.27}$$

A schematic of the CRL follows:

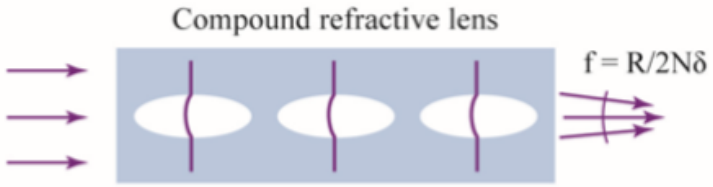

Figure 1.5: Compound Refractive Lens. Reproduced from Attwood and Sakdinawat [1] with permission.

A side-effect of the desired focusing effect of the CRL is the undesirable attenuation of the x-ray beam. While this is tolerable for hard x-rays (with an obvious trade-off between focusing power and transmission, the former requiring larger N, and the latter the opposite), the larger β makes the CRL not a good choice for soft x-rays [18]. Instead, soft x-ray optics typically make use of bending mechanisms not requiring passage through 'thick' materials, namely *Total External Reflection* (TER) and diffraction.

TER is another peculiarity of x-rays arising due to sub-unity refractive index, extending the inversion of direction of x-ray bending in refraction. It is the analog of TIR (Total Internal Reflection) for visible light: If x-rays are incident on a material at an angle less than the critical angle ($\theta_c = \sqrt{2\delta}$, which is typically on the order of a degree, and gets smaller with increasing photon energy [1, p. 76]) as measured from the surface of the material, they will not transmit through but instead will be efficiently reflected. The Capillary Lens is an example of an optic based on TER. It is, in its simplest form, a hollow tube which is shaped in such a way as to bend incident x-rays at different angles through one or more TERs, as the rays are incident at glancing angles on the internal surface of the capillary. Multiples of these tubes could be nested to form a polycapillary, to collect and efficiently reflect a larger part of the incident beam. Capillary lenses could be used in a wide range of x-ray energies, generally 1-100 keV [19].

Diffraction is another mechanism leveraged by some x-ray optics. One such optic, widely used in soft x-ray microscopy, is the *Fresnel Zone Plate* lens. The zone plate consists of a series of concentric, typically circular, x-ray transparent slits ("zones", indexed by $n = 1...N$, with r_n denoting zone n's radius) with opaque regions separating the zones. The zones get smaller and smaller with increasing radii, so that the first order diffraction peaks from all zones coincide. (The zeroth order is discarded, blocked by a pinhole termed the *Order Sorting Aperture*, or OSA for short.) For a full treatment of the zone plate, the reader is referred to [1, section 10.6]. We will include important formulae here for reference. With $\Delta r \equiv r_N - r_{N-1}$ denoting the outer zone width, the diameter of the zone plate will be:

$$D \simeq 4N\Delta r \tag{1.28}$$

and the focal length

$$f \simeq \frac{D\Delta r}{\lambda} \simeq \frac{4N(\Delta r)^2}{\lambda} \tag{1.29}$$

Note that the focal length is wavelength-dependent. This makes the zone plate a chromatic optic: x-rays of different energies will come to focus at different distances downstream of the zone plate. For microscopy applications, this necessitates spectral filtering of the beam to achieve a small enough bandwidth.

The Numerical Aperture takes on the simple form of

$$NA \simeq \frac{\lambda}{2\Delta r} \tag{1.30}$$

The depth of focus (DoF) is then

$$\Delta z = \pm\frac{1}{2}\frac{\lambda}{NA^2} = \pm 2\frac{(\Delta r)^2}{\lambda} \tag{1.31}$$

Following the Rayleigh criterion $\Delta r_{Rayl.} = 0.61\lambda/NA$, we find

$$\Delta r_{Rayl.} = 1.22\Delta r \tag{1.32}$$

for the Rayleigh resolution of a zone plate. In other words, the resolution of the zone plate is independent of the wavelength and is approximately the same as the width of its outermost zone. With lithography techniques used to fabricate zone plates advancing over the last few years, zone plates have established themselves as some of the highest resolution x-ray optics.

In addition to the first order diffraction peak, higher orders may also be used, as seen in Fig. 1.6.

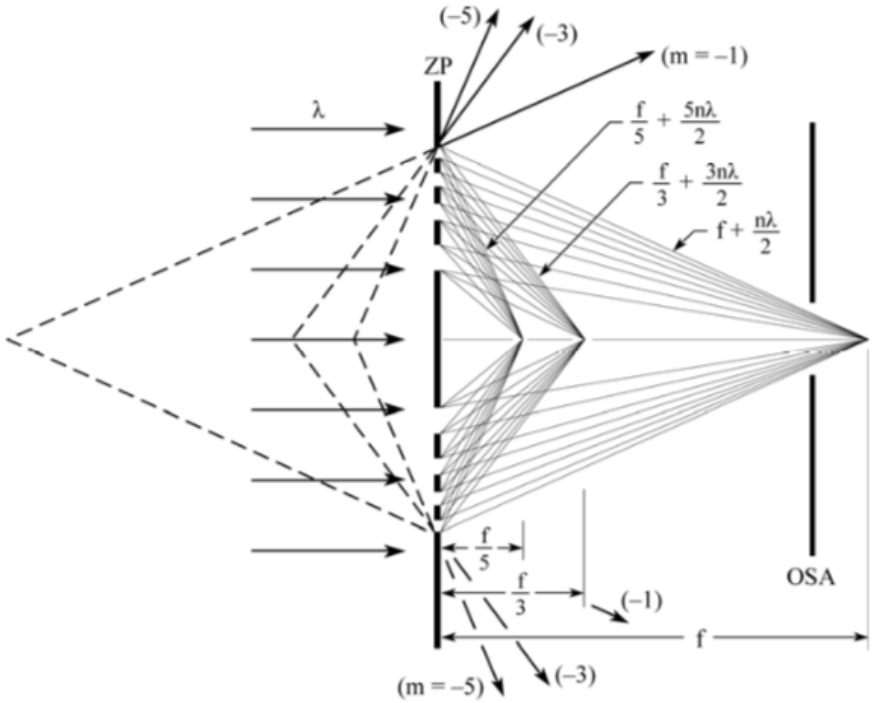

Figure 1.6: Various orders of a Fresnel Zone Plate Lens. Reproduced from Attwood and Sakdinawat [1] with permission.

Higher orders have smaller focal length and can thus achieve better resolution; but this comes at the cost of stricter bandwidth requirements due to chromatic nature of the optic, and otherwise reduced efficiency, since higher diffraction orders are of lower intensity. In general, half of the incident power is typically absorbed by the opaque region of the zone

plate, a quarter goes into the zeroth order, and odd orders contain $1/m^2\pi^2$ of the power, with m denoting the order [1, p. 477].

An important parameter in zone plate fabrication is the *aspect ratio*, which is the ratio of the depth to thickness of the thinnest zone. Due to the reduced interaction of x-rays with matter at higher x-ray energies, much higher aspect ratios are required for zone plates meant to be used in the hard x-ray regime. The difficulty in fabrication of high aspect ratio structures has traditionally been a major roadblock in availability of such zone plates, though recent advances are changing that trend [20].

1.2.2 Coherence Properties and Implications

In the last section we discussed the optics used to focus x-rays to a small spot. Aside from the optics, the x-ray beam itself also has a fundamental property that plays a role in this focusing. This property is called *coherence*, and is also responsible for the ability of the beam to form interference patterns. Mathematically, it is the degree to which the phase of the beam at two distinct points in space (or time) are correlated. It could be formalized through the normalized *complex degree of coherence*:

$$\mu_{12} = \frac{\langle E_1(t)E_2^*(t)\rangle}{\sqrt{\langle |E_1|^2\rangle}\sqrt{\langle |E_2|^2\rangle}} \tag{1.33}$$

Here, E_1 and E_2 are the complex-valued scalar electric fields at points 1 and 2. The numerator is called the *mutual coherence function* and the denominator serves the purpose of normalization. (In a more general form, one could include a time delay between points 1 and 2 to measure temporal effects in addition to the current spatial form.) The function μ_{12} takes on a value of 1 for full coherence between points 1 and 2, and 0 for complete incoherence.

Coherence is typically discussed in two different forms: *transverse* (perpendicular to the direction of propagation) and *longitudinal* (in the direction of propagation), with the latter sometimes referred to as temporal coherence, since passage of time is associated with propagation.

In the direction of propagation, one can imagine the phase relationship breaking down due to a finite bandwidth in the beam, corresponding to the wavelength range $\Delta\lambda$. Then the spectral components at either end of the bandwidth would eventually be out of phase by 180 degrees, as illustrated in Fig. 1.7. The length over which this happens is referred to as the *temporal* or *longitudinal coherence length*, denoted by l_{coh}. If it takes N_{coh} cycles for the shorter wavelength, λ, to reach this length (thus $l_{coh} = N_{coh}\lambda$), then it would take $N_{coh} - 1/2$ cycles for the longer wavelength (and thus $l_{coh} = [N_{coh} - 1/2][\lambda + \Delta\lambda]$). Equating the two, we find

$$\boxed{l_{coh} = \frac{\lambda^2}{2\Delta\lambda}} \tag{1.34}$$

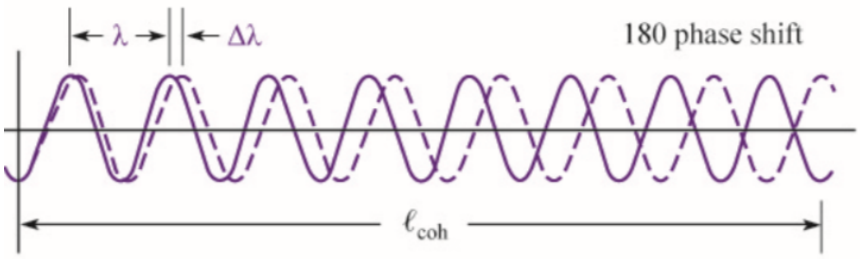

Figure 1.7: Phase relationships losing correlation over time due to spectral bandwidth. Reproduced from Attwood and Sakdinawat [1] with permission.

Even if the bandwidth of the source is infinitesimally narrow, different points on a wavefront may still not be perfectly phase-correlated in the transverse direction. To investigate this, we imagine a converging (or diverging) beam, and start by applying the Heisenberg Uncertainty Principle to the position-momentum pair:

$$\Delta \mathbf{x} \cdot \Delta \mathbf{p} \geq \hbar/2 \tag{1.35}$$

Assuming small bandwidth, the uncertainty in momentum would be due to the uncertainty in the angle θ; thus $|\Delta \mathbf{p}| = \hbar k \Delta\theta$ in the small-angle approximation. We then have:

$$\Delta x \cdot \hbar k \Delta\theta \geq \hbar/2 \tag{1.36}$$

Substituting $k = 2\pi/\lambda$ and simplifying, we find

$$\Delta x \cdot \Delta\theta \geq \lambda/4\pi \tag{1.37}$$

Letting d denote the size of the source and θ the half-angle of beam divergence, we arrive at

$$\boxed{d \cdot \theta \geq \lambda/2\pi} \tag{1.38}$$

The equality limiting case of 1.38 corresponds to a perfectly coherent beam; and a beam satisfying this condition is said to be *diffraction limited*. (This form of 1.38 with the numerical factor $1/2\pi$ is for d and θ representing the rms values of a Gaussian beam. Other metrics would result in different factors, such as roughly $1/2$ for FWHM. [1, p. 117]). Thus, a fully coherent beam converging at an angle θ will not focus to an infinitesimal point, but to a spot of size d as determined by this equality. Partial coherence of the beam will broaden the spot (and the beam) for the same angle.

The *transverse coherence length* is a measure of the portion of the beam cross-section still maintaining phase correlations, and is a function of z, the propagation distance away from the focal plane. To quantify it, we start with the equality case and replace θ with $l_{transverse}/z$ (in small-angle approximation), arriving at

$$\boxed{l_{transverse} = \frac{z\lambda}{2\pi d}} \tag{1.39}$$

Aside from its implications on focusing the beam, coherence also has consequences in how an optical system transfers the contrast of features in the sample under study to the image formed by the system. (The function that measures this transfer as a function of spatial frequencies on the sample, in magnitude, is the *Modulation Transfer Function*.) Intuitively, one can imagine that smaller features on a sample would scatter incident photons at larger angles (just like a smaller slit in the single-slit experiment results in peaks forming at larger angles.) In order for the imaging system to incorporate these higher spatial frequencies in the final image, the imaging system needs to capture these photons scattered at larger angles. Now, assuming that the objective NA of the system is fixed, the only way to increase the scattering angle captured by the system is if the x-rays incident at each given point on the sample have a diversity of incidence angles. This corresponds to reduced coherence, since full phase correlation in a neighborhood of the incident wavefront on the sample implies a fixed angle for an incident ray. Following [21], the diversity in the angles of incident rays (or "angular wedge of plane waves") is represented by the *condenser Numerical Aperture*, or NA_{cond}, which can be incorporated into the parameter

$$\sigma \equiv \frac{NA_{cond}}{NA_{obj}} \tag{1.40}$$

to form a measure of the degree of partial coherence. In the fully coherent case, incidence angles are fixed for each ray incident at any point on the sample, corresponding to zero NA_{cond}, and thus $\sigma = 0$. As coherence is reduced, σ increases with the increase in the range of incidence angles, which enables the capture of photons scattered at higher angles by the system, conveying information about features with higher spatial frequencies. (Of course this comes at the cost of less information about lower spatial frequencies, normalized to the total number of incident photons.) This behavior is visualized in Fig. 1.8 for a few different values of partial coherence.

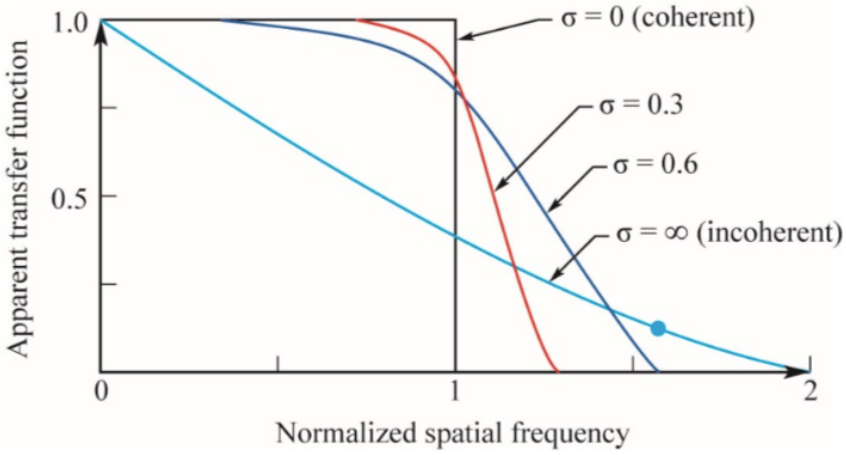

Figure 1.8: Effect of coherence on contrast transfer in an imaging system. The dot on the $\sigma = \infty$ curve corresponds to the half-Rayleigh contrast transfer of 13%, at a normalized frequency of 1.6. Reproduced from Attwood and Sakdinawat [1] with permission.

This, however, does not mean that less coherent illumination is always preferred for all types of imaging systems, even when limiting our figure of merit to resolution. Indeed, some of the highest resolution x-ray microscopes depend on the coherence of the beam. (Two examples of these are: 1-scanning techniques where the resolution depends on the size of the focal spot. These are especially useful for spectromicroscopy and are described in the next section. 2-Coherent Diffractive Imaging techniques, which are pertinent to this thesis in the form of ptychography, which requires a coherent beam and is currently highest resolution technique in x-ray microscopy. We will introduce these techniques in the next chapter.)

Another implication of coherence in the beam is a 'ringing' effect over abrupt edges in the sample, in microscopy techniques where an objective optic is used to form the image. (Recall that coherence is also a measure of a beam's ability to interfere. This ringing is one such interference effect.) A simple way to visualize this is with a knife edge scan. Fig. 1.9 shows a numerical simulation of such a scan [21]. Full coherence resulting in too much ringing can distort the image, though it does result in increased contrast at edge-like features. On the other hand, too little coherence, while resulting in a smoother image, can broaden and blur the edge. The optimal degree of partial coherence, from this perspective, depends on the sample [1, p. 523].

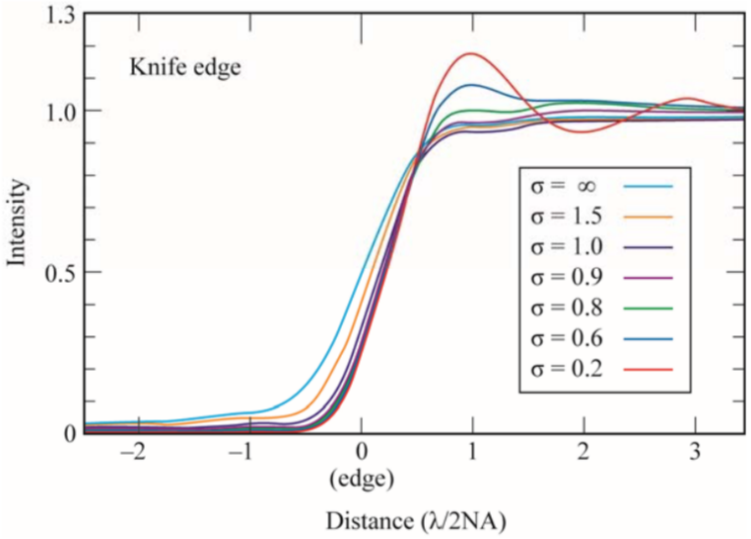

Figure 1.9: Simulation of a knife-edge scan, visualizing the effect of partial coherence on intensity distribution over an edge. Reproduced from Attwood and Sakdinawat [1] with permission.

Coherent illumination is a consequential and important topic in x-ray microscopy. Although some traditional techniques benefit from less than full coherence in the beam, other techniques, especially those at the cutting edge of x-ray microscopy, depend on the beam's coherence. Whatever the case, it is easier, given a coherent source, to reduce/destroy the beam's coherence (e.g. by means of a moving diffuser [22, p. 143]) without drastically affecting the beam's brightness, than to start with an incoherent source and achieve a coherent beam.

Although coherent sources of visible light have been commercially available for decades now, in the form of table-top and hand-held lasers, coherent sources of x-rays that are bright enough for practical microscopy are mainly large particle accelerators, in the form of synchrotrons (see [1, Chapter 5]) and Free Electron Lasers (FELs) (see [1, Chapter 6]). The work described in this thesis was conducted at Lawrence Berkeley National Lab's Advanced Light Source, a third generation synchrotron facility in Berkeley, California.

1.2.3 Full-Field and Scanning Probe Techniques

One way to categorize microscopy techniques is by region of illumination. One possibility is to illuminate the entire region of interest on a sample at once, then use an optic to focus the beam exiting the sample to form an image downstream. This is referred to as *full-field* imaging. Alternatively, in *scanning probe* microscopy techniques, the incident illumination is focused onto the sample and scanned, and the exit beam is recorded on a detector downstream and processed to form an image. In x-ray microscopy, the main traditional full-field

technique is known as *Transmission X-ray Microscopy*, or TXM [23], and the main traditional scanning probe technique is known as *Scanning Transmission X-ray Microscopy*, or STXM [24], [25].

In TXM, the incoming x-ray beam (e.g. from a sychrotron beamline) is condensed on the sample (typically using a capillary or zone plate optic), illuminating the region of interest. An objective zone plate placed directly downstream of the sample then collects the exit wave and focuses it to directly form the image on a detector downstream.

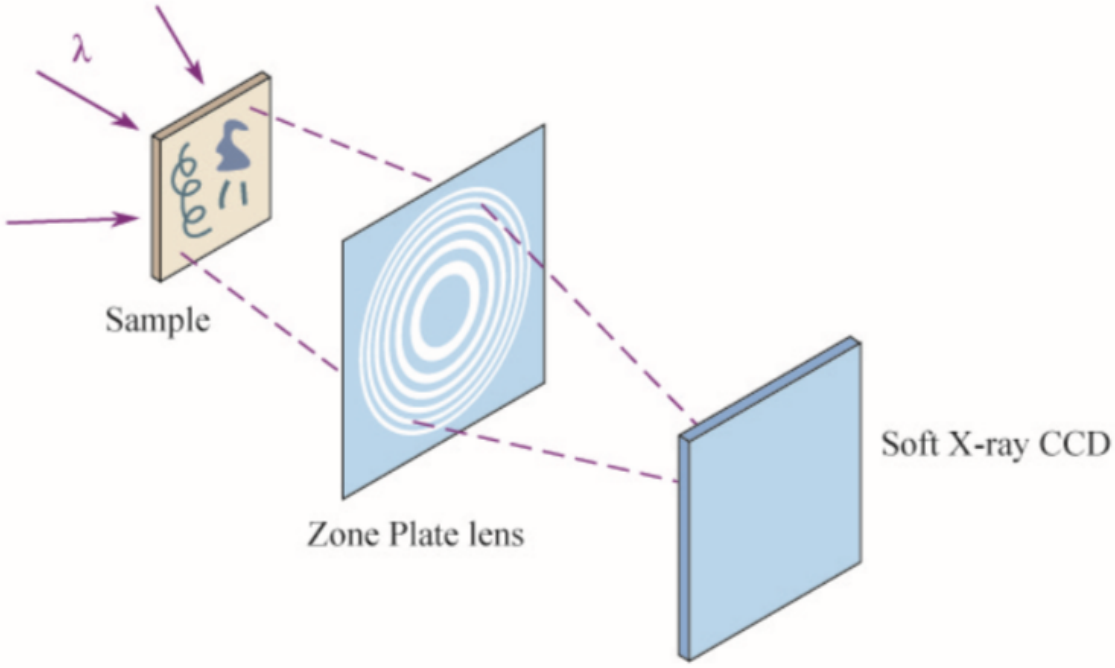

Figure 1.10: Transmission X-ray Microscope (TXM). Reproduced from Attwood and Sakdinawat [1] with permission.

In STXM, the incoming beam is focused to the smallest spot possible (when maximal resolution is desired), typically using a zone plate, and either the optic or the sample is scanned transverse to the beam direction. A single-pixel detector (such as a photodiode or PMT) records the total x-ray transmission at each relative position of sample and focused spot. A map of these transmission values is the final image. A segmented detector can be used in place of a single-pixel detector to image in darkfield mode [26].

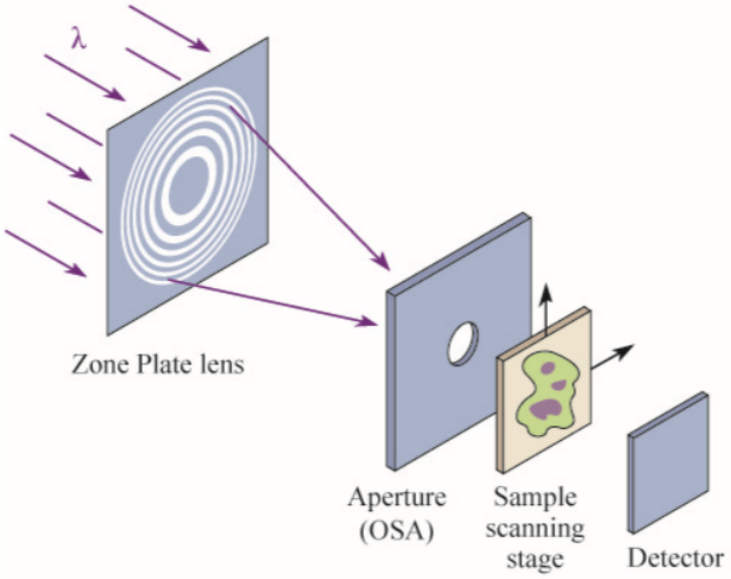

Figure 1.11: Scanning Transmission X-ray Microscope (STXM). Reproduced from Attwood and Sakdinawat [1] with permission.

The scanning nature of STXM adds a significant amount of overhead in time needed to form an image, as opposed to TXM where the entire image is formed at once. This can become especially important if dynamics in the sample are of interest. However, there are other factors that can, depending on the experiment, make STXM more desirable. One is beam damage: since TXM uses an objective zone plate, typically having around 10% efficiency, ten times as many photons need to interact with the sample to form a comparable image to that formed through STXM, leading to increased radiation damage. Additionally, in TXM, due to the nature of available x-ray beams and optics, the condensed x-ray beam on the sample tends to be non-uniform [27], which, aside from imprinting the non-uniformity on the final image, makes quantitative spectromicroscopy difficult. (Spectromicroscopy involves extraction of chemical information by changing the x-ray energy in the neighborhood of an absorption edge, and analyzing the change in x-ray transmission. More on this in a later chapter.) This is not an issue with STXM since the entire beam is focused onto a small spot, resulting in consistent illumination.

Another difference between TXM and STXM is their relationship with beam coherence. In STXM, the resolution is determined by the size of the spot formed on the sample, which is optimal in a fully coherent beam. TXM, on the other hand, utilizes an objective zone plate to form the image, and it thus benefits from improved resolution in a less coherent beam, as visualized in Fig. 1.8 [1, p. 541].

1.2.4 Limitations of Traditional Techniques

Traditional x-ray microscopy techniques, such as those discussed so far, have two factors in common: the final image contains only intensity information about the sample (phase information is lost), and the image is constrained (e.g. in resolution) by limitations in the fabrication of the optics (among other constrains). It is desirable to overcome these barriers. This serves as the motivation for the development of a new class of imaging techniques, known collectively as Coherent Diffractive Imaging (or Coherent Diffraction Imaging), discussed in the next chapter.

Chapter 2

Coherent Diffractive Imaging Techniques for X-ray Microscopy

2.1 Resolution, the Problem of a Sample's Phase, and the Phase Problem

As discussed in the previous chapter, we are motivated, in designing new imaging systems, to bypass the limitations on resolution imposed by image-forming x-ray optics. Furthermore, we saw that a sample under study will change the phase of the incident x-ray beam, in addition to attenuating its intensity. Images produced by traditional microscopy techniques, such as those described in section 1.2.3, map the attenuation, but convey no information about the phase change.

2.1.1 X-ray Holography and the Problem of a Sample's Phase

Traditionally, holography has filled in this gap to provide phase information about the sample, first demonstrated for electrons by Gabor [28], and later for x-rays [29, 30, 31, 32]. X-ray holography originally involved 'splitting' the beam into two, one which is incident on (and interacts with) the sample, and another, the *reference beam*, which bypasses the sample. (The splitting can either be a complete off-axis separation, or the reference beam can simply be the portion of the incident beam that passes through the sample relatively undisturbed. The latter is known as *inline* holography.) The two beams are then made to interfere, encoding phase information into intensity, which is recorded on a detector such as photographic film/transparency. This recorded pattern, known as a *hologram*, can then be illuminated by the reference wave in the absence of the sample, recreating the sample's image. Early results were limited in resolution by the photographic film resolution; later on, magnification allowed by projection from a point source removed this bottleneck, and set the source size as the limit [7]. This has allowed resolution as high as 0.5Å in the special case of a fluorescent atom in a crystal acting as the point source [33].

2.1.2 The Phase Problem

The purpose of the reference beam in holography is to provide a baseline for the phase of the beam interacting with the sample and encode it into intensity modulation through interference. Interference with a reference beam would not be needed if we could know the phase of the the latter beam in a more direct way. If the x-ray beam interacting with the sample were coherent, the exit wave propagating to far-field (with this propagation working as a Fourier Transform) would form a speckle pattern on the detector. (Incoherence in the beam, corresponding to a range of incident angles on the sample at any point, would blur these speckles and effectively reduce the amount of information recorded.) If the detector could record the complex-valued propagated beam, finding the sample's imprint on the incident beam would be as simple as performing an inverse Fourier Transform. Unfortunately, detectors record intensity only; phase information of the propagated beam is lost. This inability to directly solve for the complex-valued sample function due to the loss of phase information in recorded data is referred to as *the phase problem*.

2.2 X-ray CDI

Although no phase information is recorded at the detector, all hope is not lost: some phase information of the exit wave, through propagation, is encoded into intensity and recorded. The class of computational imaging techniques that attempt to reconstruct the sample using this recorded information give rise to Coherent Diffractive Imaging, or CDI for short.

2.2.1 Single-shot CDI

The field of Coherent Diffractive Imaging has its roots in what is now known as *single-shot* CDI [1]. This is where we start our exploration of CDI.

The sample is prepared and placed in the path of an incident beam of coherent x-rays. After interacting with the sample, the beam diffracts and propagates to the far-field, where the intensity is recorded on an array detector (typically a CCD, either direct-detection or used with a scintillator), as visualized in Figure 2.1. (There is usually a beamstop present as well, to block the direct beam that passes through the sample undisturbed.) Let ψ be a complex function denoting the electric field of the beam incident on the sample, and O, the 'object function', the complex function whose magnitude and phase correspond, respectively, to attenuation and phase change at each point on the sample (or object). Then the *exit wave* immediately downstream of the sample would be $\psi \cdot O$, and the electric field at the detector in the far-field would be $F\{\psi \cdot O\}$, where F denotes the Fourier transform and represents far-field propagation. The detector then records the intensity of the beam at this point: $I = |F\{\psi \cdot O\}|^2$ The goal, then, is to solve for O, given the recorded I.

[1] To this day in the x-ray microscopy community, the acronym CDI is sometimes used to refer to single-shot CDI, rather than the class of diffractive imaging techniques.

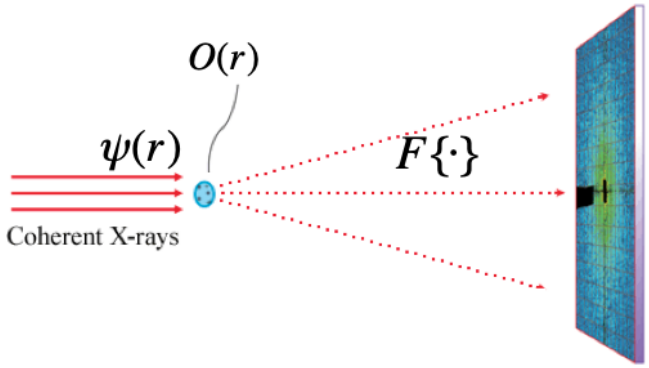

Figure 2.1: Single-shot CDI. Modified from `http://www.esrf.eu/news/spotlight/spotlight54/XDM`

The first progress towards achieving this goal came in the 1970s, when Gerchberg and Saxton introduced an algorithm to address a similar class of phase-retrieval problems, but with intensity measurements taken in both the real ('imaging') and Fourier ('diffraction') domains [34]. (They proposed their method mainly for electron microscopy, but commented that it might be useful in visible light microscopy and x-ray crystallography as well.) Later, Fienup modified and improved this algorithm to require only one recorded intensity, in the Fourier domain [35]. (Interestingly, the context he mentioned was how "atmospheric turbulence limits the resolution of an image obtained through a large telescope.") Although modern algorithms can be much more complicated and involved, there is value, for the purpose of gaining intuition, in considering these initial algorithms that gave birth to CDI, starting with Gerchberg-Saxton's iterative error-reduction algorithm:

1. Start with a complex object (sample) function whose intensity is the measured intensity and whose phase is a random initial guess.
2. Fourier transform this function to arrive at the detector plane (far-field).
3. Keep the phase, but replace intensity with the measured diffraction intensity.
4. Inverse Fourier transform to arrive back at the object plane.
5. Keep the phase, but replace the intensity with the object's measured intensity.
6. Repeat steps 2-5 until convergence.

Fienup's original insight was to circumvent the requirement of knowledge of the object's intensity by applying constraints to the reconstructed object function at step 5 of each iteration. The constraints were that the reconstructed object should be non-negative throughout, and that the reconstructed object's diameter should be contained to the object's known diameter, which is half the diameter of its autocorrelation. (The latter is now known as the 'finite support' constraint.)

This method of solving the phase problem generally worked well; but the solution was not unique and depended on the initial object guess. In 1982, Bates demonstrated that effective uniqueness is 'almost always' guaranteed as long as the Fourier domain is properly oversampled, at the Nyquist rate [36].

Although developments in CDI were ongoing since early 1970s, no CDI technique was demonstrated in the context of x-ray imaging until 1999, when Miao *et al.* successfully used x-rays of 1.7nm wavelength to image gold nanoparticles of 100nm in diameter at a resolution of 75nm [37] (Fig. 2.2).

Figure 2.2: First demonstration of single-shot CDI with x-rays. the recorded diffraction pattern in logarithmic scale (left), reconstructed object (center), and SEM image for reference (right). Reproduced from [37] with permission.

Since this first demonstration, many advances have been made in single-shot CDI. New algorithms have been developed, including Elser's 'Difference Map' [38] and Marchesini's 'Shrinkwrap' [39]; Chapman *et al.* extended the technique to 3D [40].

2.2.2 Beyond Single-shot

Perhaps more important than the success of single-shot CDI in the x-ray community in its own right is that it has led to a growth and branching out of CDI into more specialized CDI techniques. The particular technique of choice in any context would depend on the x-ray energy, type of sample, information desired, and experimental limitations. In general, these other CDI techniques have all but superseded single-shot CDI, except in cases where experimental limitations necessitate single-shot CDI, such as in diffraction-before-destruction experiments at FELs, where there is only one chance at measuring the sample before it is destroyed by the intense beam (e.g. [41]). In this section, we will briefly discuss some of the CDI techniques used in the x-ray world, before going in depth into ptychography, the CDI technique pertinent to this thesis.

As was mentioned, one of the motivations in moving beyond traditional x-ray imaging techniques into CDI (in addition to obtaining phase information) is to gain higher resolution, not constrained by limitations in x-ray optics fabrication. In single-shot CDI, resolution is

dependent on the scattering angle of the most diffracted photons captured by the detector. For the vast majority of the x-ray spectrum, x-ray interaction with matter is too weak for the detector NA to be a limiting factor. For very low energy x-rays, crossing into the Extreme Ultraviolet regime, however, photon scattering angles may become too large for many experimental setups. First developed by Zheng *et al.* in the visible light regime [42], **Fourier Ptychographic Microscopy** (FPM for short) addresses this problem by tilting the angle of illumination and recording multiple measurements at different angles, effectively increasing the total NA of the imaging system. This technique has since been implemented in the EUV regime in the SHARP instrument at the Advanced Light Source [43, 44].

In crystallography, hard x-rays interact with the crystalline lattice, and diffract to far-field to form Bragg peaks, giving rise to the reciprocal lattice. Strains due to imperfections in the crystal would break local symmetry, resulting in a complex diffraction pattern taking shape at each reciprocal lattice point. **Bragg CDI** applies the CDI technique to phase this diffraction pattern, in order to map the strain in the crystal [45, 46].

One of the requirements in successful implementation of single-shot CDI is the isolation of the sample. This is needed both in order to satisfy the oversampling requirement, and to enable the imposition of the finite-support constraint in the reconstruction algorithm. Experimental implementation of this sample isolation requirement can be very difficult in many cases. **Keyhole CDI** [47] (KCDI for short) obviates this need by focusing the illumination. The sample is placed downstream of the focal plane. The divergent exit wave, having interacted with the sample, then propagates downstream to the detector, effectively 'magnifying' the diffraction pattern. The diffracted wave at the detector plane is then related to the exit wave according to the Fresnel formalism, enabling the phasing of the recorded diffraction pattern intensity [48].

For more on x-ray CDI, the reader is referred to [49, 50, 51].

2.3 Ptychography

Similarly to KCDI, ptychography addresses the isolation requirement by focusing the beam on the sample. Imaging of arbitrarily large fields-of-view are then enabled by relative scanning of the illumination and the sample, with overlap of adjacent scan positions, as diffraction patterns are recorded at each position. (From the standpoint of experimental setup, then, ptychography can be viewed as a combination of STXM and CDI.) Ptychography was first proposed by Hoppe and Hegerl in 1969-70 for electron microscopy [52, 53] [2]. The first x-ray demonstration took place in 1996 by Chapman in the form of Wigner distribution deconvolution [54]. (This method eases the reconstruction process by linearizing the phase retrieval problem, enabled by highly dense scan patterns.) It wasn't until Rodenburg and Faulkner's iterative algorithm in 2004 [55, 56] (which came to be known as the Ptychographical Iterative Engine or PIE), and its demonstration for x-rays [57], that x-ray ptychography, in its currently recognizable form, started to flourish. This scheme requires much less overlap,

[2] Hoppe and Hegerl also proposed the name 'ptychography', from 'πτυχή', Greek for fold/crumple.

but is more computationally expensive. (See [58] for an analysis of overlap with respect to quality and dose in PIE.) But before it could rise to claim its place as the highest resolution workhorse of x-ray microscopy, it first had to resolve issues due to model mismatch, which plagued the early results. We'll discuss this next. For a more complete review of the development of ptychography, the reader is referred to [59, 60].

2.3.1 Simultaneous Recovery of Experimental Parameters

In its basic form, the ptychography forward model needed to make a few assumptions about the experimental setup. These included accurate knowledge of scan positions, full coherence of the beam, and the profile of the illumination incident on the sample. Any mismatch between the assumptions and the experiment would result in a degradation of the quality of the reconstruction. Problems of this kind were not easily addressable in single-shot CDI except on the experimental side; but the redundancy in information in ptychography due to the overlap of illumination in neighboring scan positions enabled algorithmic developments to treat other experimental parameters not as assumptions, but as unknowns, and to solve for them simultaneously along with the sample.

Probe Retrieval

Perhaps the most pressing model mismatch issue had to do with the illumination profile: In their initial forms, single-shot CDI and ptychography depended on accurate a priori knowledge of the illumination; and "while the visible light results were of decent quality, the x-ray case suffered heavily from imperfections in the illumination" [59]. In 2008, Thibault et al built on the difference map algorithm [38] to demonstrate simultaneous recovery of the complex-valued illumination profile at the sample (the 'probe') along with the complex-valued sample itself [61]. Improvement in reconstruction quality of the sample is clearly visible when the probe is refined as opposed to kept fixed at estimation based on geometry, as seen in Fig. 2.3.

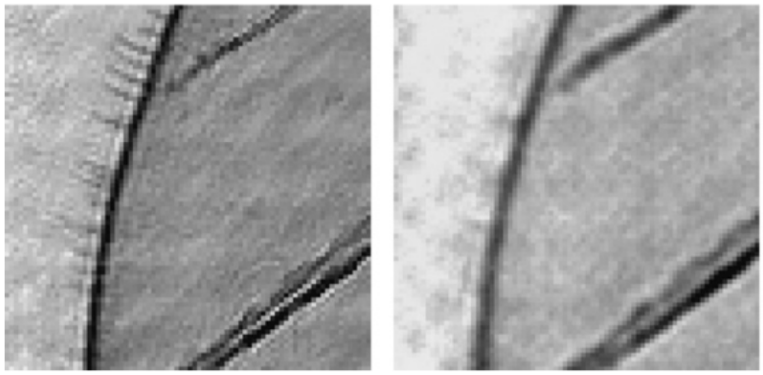

Figure 2.3: Effect of probe retrieval on amplitude of the reconstructed sample, as shown by Thibault et al. The probe is initiated as the exit waveform of a 200um pinhole propagated 1.1mm downstream, and is refined through iterations (left) or kept fixed (right). Reproduced from [61] with permission.

They applied this method to produce high-resolution images of a zone plate and showed that the retrieved probe, when propagated to the detector plane, has a magnitude that closely matches the recorded probe with no sample in the way [62]. Other than improving the quality and accuracy of the reconstructed sample, this reliability of the retrieved probe is of importance in its own right: aside from microscopy experiments, where the goal is to characterize the sample under study, there are other circumstances where one might seek to characterize a complex wavefield (e.g. new sources such as FELs whose beams need to be characterized to interpret experimental results [63]); probe retrieval allows this to be done with ptychography, ideally using a highly scattering sample (see, for example, [64] by Kewish et al.)

Extensions to other ptychography algorithms have also been developed to allow probe retrieval, such as ePIE for the PIE algorithm [65].

Partial Coherence Correction

As was mentioned earlier, all CDI techniques, including ptychography, rely on coherence of the beam; deviations from perfect coherence result in the blurring of the speckles carrying information in the diffraction patterns (mathematically, this corresponds to convolving the mutual coherence function of the beam with the coherent result.) Modern x-ray synchrotron facilities have succeeded in producing highly coherent beams at brightness levels sufficient for imaging applications. Nevertheless, no source is perfectly coherent; and increased coherence at a beamline comes at the cost of reduced flux due to spatial filtering. Finite partial coherence, traditionally not accounted for in the ptychography forward model, can degrade the reconstruction quality. This problem was addressed by Thibault et al in 2013 by incorporating partial coherence in the ptychography forward model as an incoherent summation of various coherent modes, which are then solved for, resulting in a successful reconstruc-

tion of the sample, as well as serving to characterize the illumination [66]. Later, Enders et al demonstrated successful reconstructions using a broad-bandwidth beam [67]. Recently, Chang et al have put forth another approach to address partial coherence correction, by gradient decomposition of the probe [68].

Fig. 2.4 shows an example of increased reconstruction quality due to partial coherence correction.

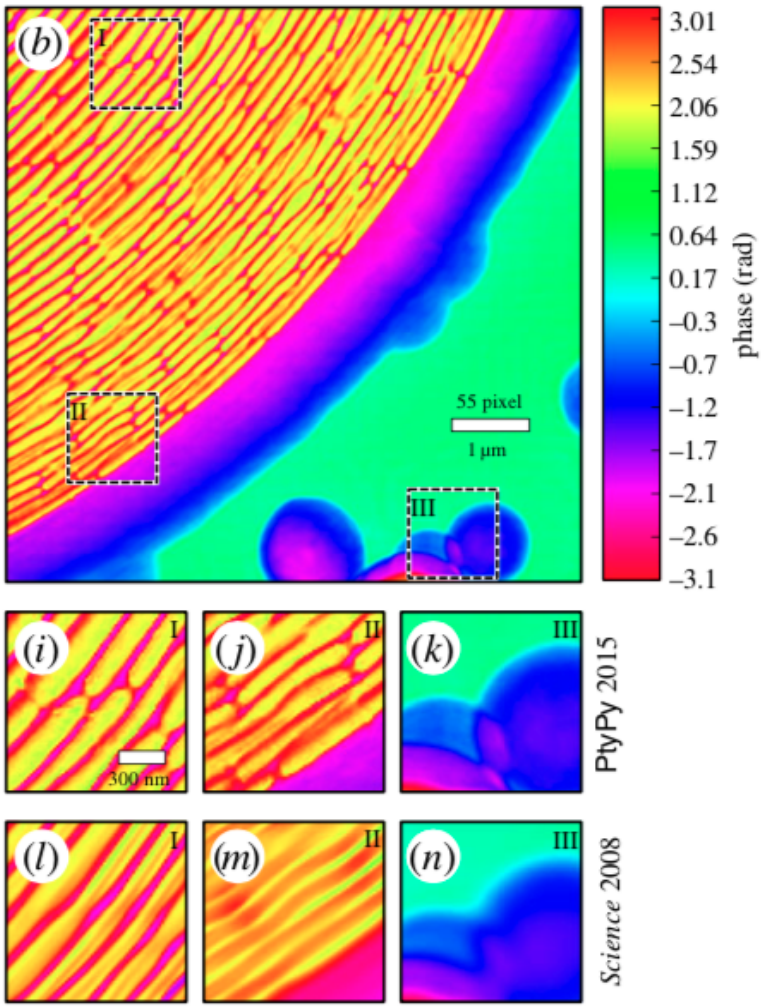

Figure 2.4: Effect of partial coherence correction on the phase of the reconstructed sample (part of a zone plate in this case.) [i,j,k] and [l,m,n] show reconstructions of areas I,II, and III with and without partial coherence correction, respectively. Reproduced from [69] under Creative Commons license: `http://creativecommons.org/licenses/by/4.0`

Position Correction

One of the parameters input into any ptychography reconstruction algorithm is the set of real-space coordinates (at the sample plane) at which diffraction patterns were acquired. The accuracy with which stages can be positioned (or with which a sensor can report the positions) may not be sufficiently high. Additionally, even with highly accurate and precise positioning, system-wide drift over the duration of a ptychography scan could similarly lead to inaccurate position data, degrading reconstruction and reducing resolution.

Several approaches have been developed to address this issue during the optimization iterations of a ptychography solver. Although not fully successful in correcting all positional inaccuracies, they have demonstrated significant improvements in reducing position errors and leading to increased resolution. See for example [70, 71, 72].

2.3.2 Software Packages

The success of ptychography as a reliable microscopy technique providing highest resolutions possible has resulted in its adoption worldwide at modern synchrotron facilities. A few software packages have been developed, incorporating various reconstruction algorithms. Here we list a few of the popular options.

SHARP

Developed at Lawrence Berkeley National Lab by Marchesini et al, SHARP (for Scalable Heterogeneous Adaptive Real-time Ptychography) utilizes parallelization over GPU cores to accelerate reconstruction [73]. It allows for probe retrieval, background retrieval, and partial coherence correction through gradient decomposition of the probe. More information is available at `https://www.camera.lbl.gov/sharp`.

PtyPy

Compiled by Thibault and Enders, PtyPy is an open-source python-based ptychography package [69]. It is parallelizable over CPU. It relies on the difference map algorithm and incorporates maximum likelihood refinement [74], and allows for real-time reconstruction as data is acquired. For more information, visit the homepage at `http://ptycho.github.io/ptypy`.

PyNX

PyNX (Python tools for Nano-structures Xtallography) [75] is another package available under an open source license, from the European Synchrotron Radiation Facility. More information is available at `http://www.esrf.eu/computing/scientific/PyNX/README.html`.

PtychoLib

Developed by Nashed et al at Argonne National Lab, PtychoLib is another open source library utilizing parallel processing over GPU cores [76]. More information is hosted at `https://www.mcs.anl.gov/~ynashed/2018/10/23/Software.html` at the time of this writing.

2.3.3 Combination with Tomography

Since long ago, the Radon transform has enabled the formation of a three dimensional image of a sample under study by combining multiple projection images from a range of angles (ideally covering the full 180 degrees.) Tomographic imaging can be a particular strength of x-rays due to their long absorption lengths, enabling study of thicker samples. Ptychography has allowed x-ray tomography to be performed at even higher resolutions (see, for example, [77] by Holler et al.) Combining ptycho-tomography with spectroscopy, another strength of x-rays, Yu et al have recently demonstrated chemical maps with a 3D spatial resolution of 11nm [78].

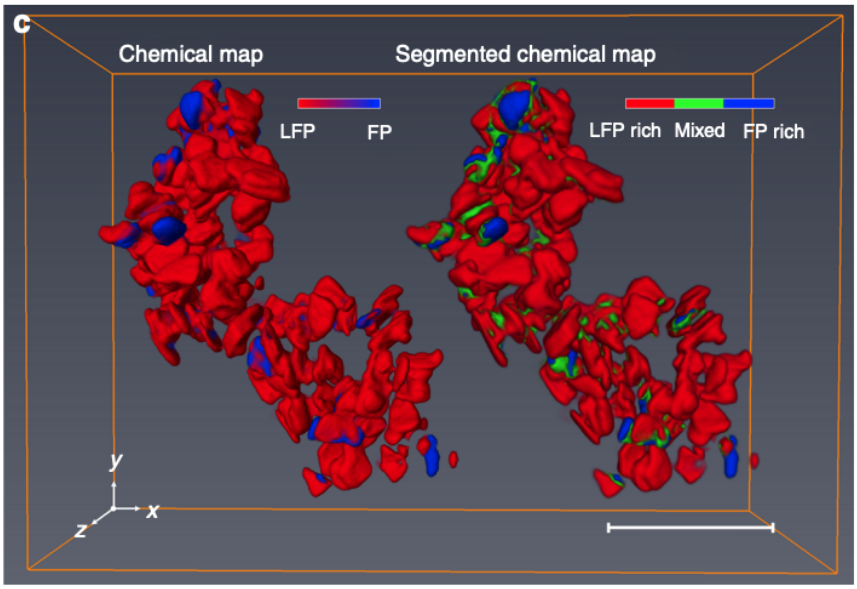

Figure 2.5: Chemical information at high spatial resolution in 3D: chemical map of a mixed-phase battery material (left) and its segmentation into three chemical phases (right). Scale bar is 500nm. Reproduced from [78] under Creative Commons license: `http://creativecommons.org/licenses/by/4.0`

Practical demonstrations of x-ray ptycho-tomography have so far involved performing ptychography scans and reconstructions in 2D at individual angles, followed by a traditional tomographic reconstruction. Although not yet demonstrated experimentally, a new concept has been proposed and demonstrated in simulation by Gürsoy, to bypass individual 2D

ptychographic reconstructions, to instead use all the diffraction patterns at all angles at once in a single 3D ptycho-tomographic reconstruction [79]. This approach would have the advantage of relaxing the overlap requirement in 2D, instead relying on the 3D bulk of the sample to impose additional constraints [80]. Data collection time is thus significantly reduced, as is the radiation dose imparted on the sample.

2.4 At the Advanced Light Source

The Advanced Light Source (ALS) is a third generation synchrotron facility built on the site of the decommissioned cyclotron at Lawrence Berkeley National Lab in Berkeley, where the cyclotron was invented by Ernest Lawrence. The ALS started operation in 1993, and has since been home to many x-ray microscopes, including the full-field instruments XM1 and XM2, and multiple STXM instruments.

Since the early implementations of single-shot x-ray CDI, many experiments were conducted at the ALS to explore its viability as a user-accessible regular technique. (A successful example was mentioned earlier in this chapter: biological imaging with a yeast cell sample, by Shapiro et al [81], as shown in Fig. 2.6.)

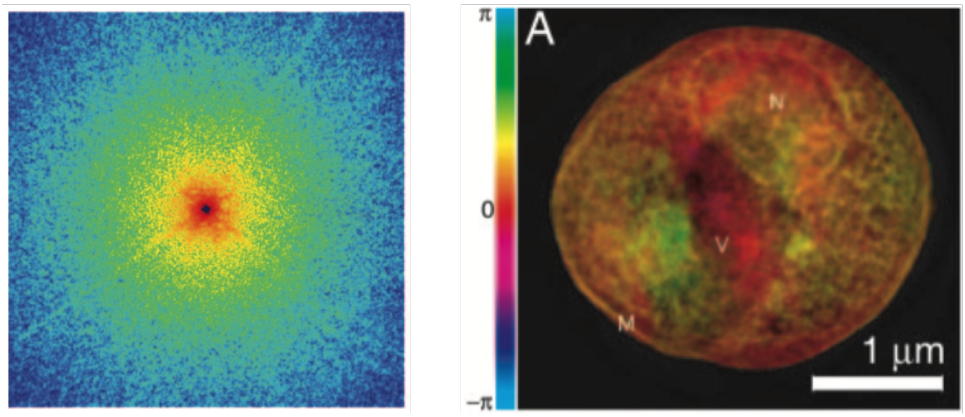

Figure 2.6: The diffraction pattern collected from a frozen yeast cell during a single-shot CDI experiment (left) and the phase of the reconstruction (right). Reproduced from [81]; Copyright 2005 National Academy of Sciences.

The ptychography program at the ALS then started by building upon the already-existing STXM expertise at the ALS to develop ptychography microscopes upon the STXM instrumentation infrastructure. (This involved making various modifications, including making the instrument more precise and stable, and adding array detectors.) In addition, a proper computing infrastructure was put in place, involving a GPU cluster for reconstruction, and the development of a ptychographic reconstruction package, SHARP, mentioned in the previous section. This effort was later dubbed the Nanosurveyor program, and resulted in the

Nanosurveyor instrument [82]. The instrument was able to resolve 5nm half-period lines with 25% contrast, and gave rise to a successful user program at the ALS based on ptychographic microscopy. The chemical map of battery materials [10], mentioned earlier, was produced using this instrument, as shown in Fig. 2.7.

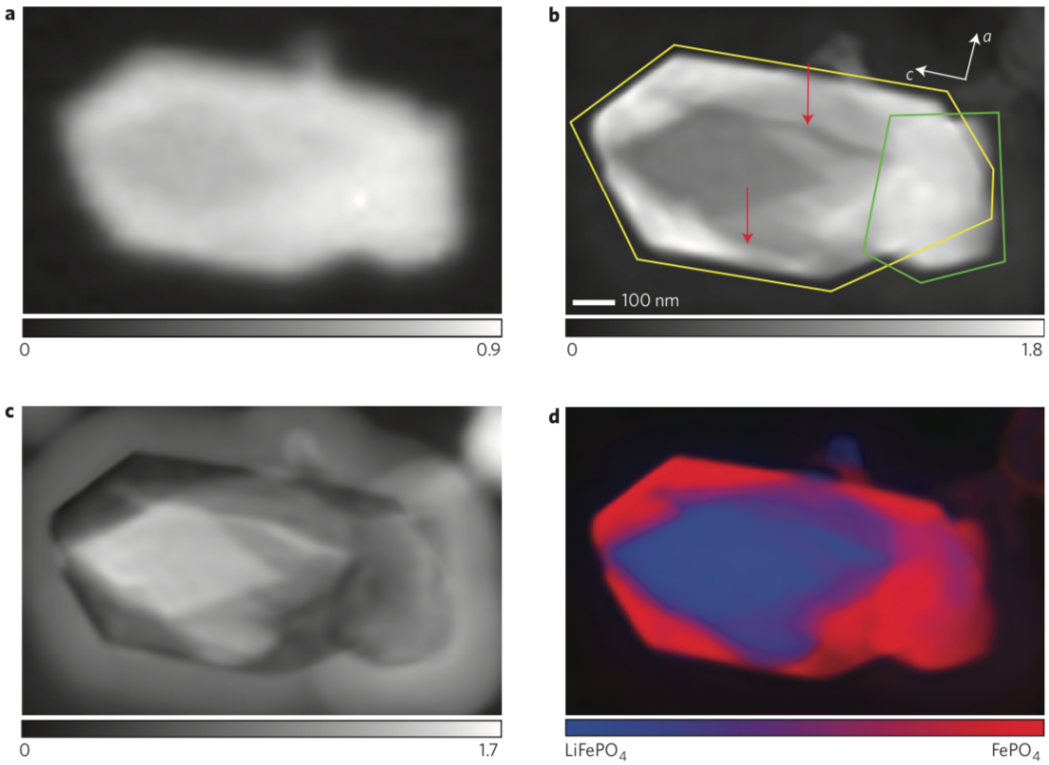

Figure 2.7: Imaging of a battery nanoparticle: STXM (a), ptychography magnitude (b) and phase (c), and chemical map based on a stack of x-ray energies (d). Reproduced from [10] with permission.

The success of this program partly led to the development of the COSMIC (Coherent Scattering and Microscopy) facility [83] at the Advanced Light Source, partly involving the development of a new compact, ultrastable ptychography microscope. We will discuss this instrument in the next chapter.

Chapter 3

Nanosurveyor 2

The success of the original Nanosurveyor instrument at the Advanced Light Source paved the way for furthering efforts in advancing the microscopy capabilities based on ptychography. These efforts included building a brighter beamline with an undulator source (7.0.1, known as COSMIC for Coherent Scattering and Microscopy), improving computational capacities, and indeed building a more stable, compact microscope capable of achieving highest resolutions. In this chapter, we discuss this microscope, dubbed Nanosurveyor 2.

3.1 The Instrument

3.1.1 Overall Design and Integration

Ptychography has been described as a combination or marriage of STXM and [single-shot] CDI. It is no surprise, then, that the instrumentation aspect also reflects this reality. On the surface, this combination would just involve adding an array detector to a STXM, and we're there. This was the start of the development path for initial ptychography microscopes. (The original Nanosurveyor instrument at the ALS was also developed on the infrastructure inherited from the STXM program.) The larger size of the 'traditional' STXM is ideal in allowing the versatility and flexibility called for in developing new instrumentation. But there is a price that has to be paid in return: reduced stability, in the form of drift (in long term, over minutes or hours) and vibrations (over the short term.) These are of negligible practical consequence in STXM: 1-scans are of much shorter duration due to the much lower exposure time at each point, so drift is not as pronounced; 2-STXM doesn't make use of the information in the diffraction pattern, which would be blurred by vibrations (equivalent to partial coherence.) The only effect of vibration would be a slight broadening of the beam, which is negligible in STXM, since the resolution is already much worse than diffraction limited.

A number of measures were implemented to address these and other issues.

The mechanical path length from the tip of the sample holder to the position of the

zone plate directly contributes to drift; so the guiding design philosophy was to make the instrument compact in order to reduce all mechanical path lengths and reduce drift.

When it comes to the relative scanning of the sample and the beam, there are two possibilities: to fix the beam and scan the sample, or fix the sample and scan the beam (by scanning the zone plate.) Scanning the sample has the benefit of a stationary, constant illumination profile; but if tomography is desired, the 4-axis sample stage (x,y,z, rotation) would typically be too clunky to scan quickly, and would increase the overhead in a ptychography scan (with the overhead being the time it takes to move the motor from one scan position to the next throughout the scan.) The decision was thus made to assign the scanning job to the zone plate stage, and use the 4-axis sample stage only for positioning and finding the field of view. To address the issue of uniform illumination, the zone plate is then significantly 'overfilled' so that the incoming wave appears approximately as a flat front within the scanning range of the zone plate stage. This is the same approach as in the original Nanosurveyor instrument; but one difference is that here the OSA (order sorting aperture) stage is also mounted on the zone plate scanning stage and is thus scanned with the zone plate, allowing for a much larger field of view.

To reduce the vibrations associated with the zone plate stage, the design incorporated a connecting piece of sapphire to mount the zone plate on the stage. This design element was inspired by the TEAM microscopes at NCEM (the National Center for Electron Microscopy), which similarly took advantage of the stiffness (high resonance frequency) of sapphire [84, 85]. The sample stage incorporated into the microscope was a commercial stage from an electron microscope. (Electron microscopes achieve higher resolutions than photon-based microscopes, and thus have more stringent requirements in terms of stability. This stability was relied upon in our microscope.) The zone plate scanning stage bracket is then directly rigidly attached to the sample stage.

A direct-detection x-ray CCD is then placed a few centimeters downstream of the sample stage. (Since the beam is focused to a spot tens of nanometers in diameter, the Fresnel number corresponding to a propagation of soft x-rays to a few centimeters is already well below unity, placing the detection plane in the far-field.) The detector was developed by the Detector Group at Lawrence Berkeley National Lab [86].

A photo-diode is also included immediately downstream of the sample as a secondary detector for low resolution STXM scans. It is mounted on an arm that is moved out of the way once the region of interest for high resolution ptychography has been identified. The overall mode of operation of the microscope, then, is to insert the sample, use low resolution STXM scans (by scanning the beam) to find the region of interest, change the field of view by stepping the sample stage and repeat the previous step if necessary, and finally expose the CCD by retracting the photo-diode, and do a high resolution ptychography scan.

Fig. 3.1 illustrates the overall design of the instrument.

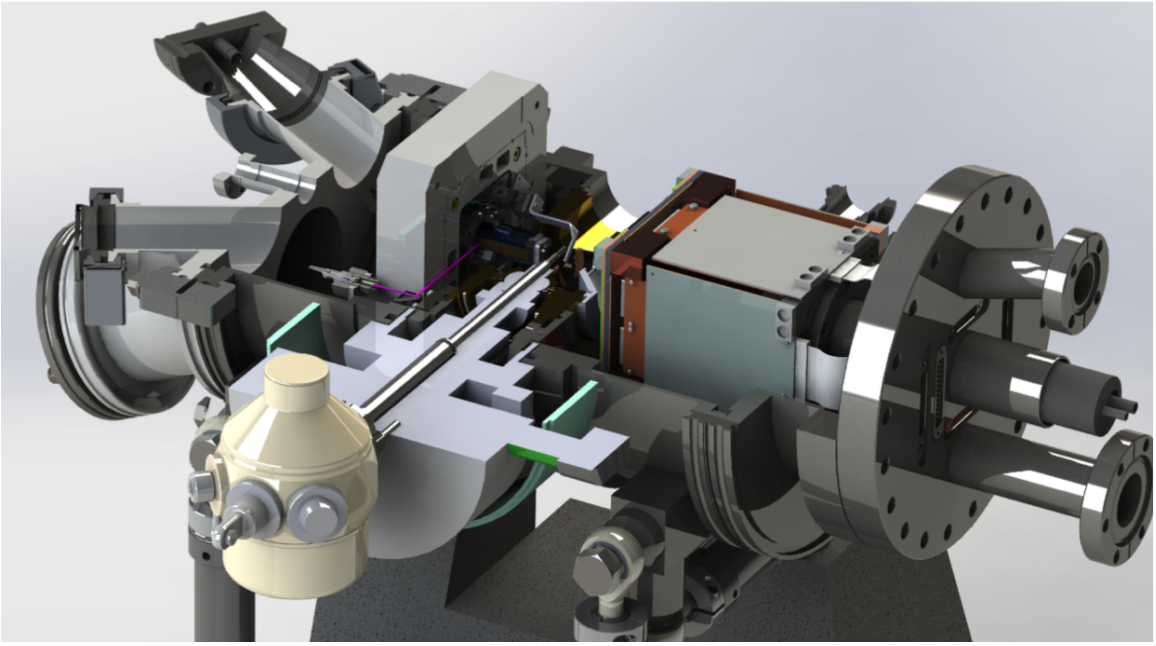

Figure 3.1: A CAD drawing, illustrating the overall design of the microscope, including the zone plate stage upstream (left), sample stage in the middle, and the CCD downstream.

Next, we will discuss the stages in more detail.

3.1.2 Zone plate Scanning Stage

The zone plate requires 3 degrees of freedom: x-y to scan the beam on the sample, and z, to coincide the focal plane with the sample, and adjust with the changing x-ray energy (since the zone plate is a chromatic optic.) The requirements for x-y are, however, quite different than the requirements for z: scanning the beam needs to be done with nanometer precision at high frequency over a small range (tens of microns); whereas comparatively infrequent stepping in the z direction with changing energies has larger tolerance for positioning (e.g. following Eq. 1.31, the depth-of-focus for a 45nm zone plate for x-rays of 1nm wavelength is: $\Delta z = \pm 2\frac{(\Delta r)^2}{\lambda} = \pm 2\frac{(45nm)^2}{1nm} = \pm 4.05\mu m$), but requires a large range (according to Eq. 1.29, $f \simeq \frac{D\Delta r}{\lambda}$, the focal length of the same zone plate, given a typical diameter of $240\mu m$, at the two ends of the soft x-ray regime, would differ by more than a centimeter.)

To best meet these requirements, two separate stages were used. A commercial piezo flexure stage from Physik Instrumente (PI) with a range of 100 microns in both x and y was chosen for fast, precise scanning. To position the zone plate in z, an elongated hexagonal piece of sapphire (mentioned earlier, chosen for stiffness), at one end of which the zone plate is attached, is placed, on its lower oblique faces, on four piezo sheer actuators (PICA Shear, also from PI.) The bracket holding these actuators is then mounted on the x-y stage. To drive the sheer actuators, a one-sided sawtooth pattern sequence with an amplitude of

10V is generated using a PCI card on a computer, which is then amplified to 500V, and drives all four actuators synchronously. The change in voltage has the effect of sheering the actuators laterally in the z direction. At every cycle of the sequence, the slow-moving portion of the one-sided sawtooth pattern drags the sapphire along with the actuator by about half a micron, while the fast-moving portion slips without moving the sapphire. Thus, an arbitrary distance, up to the full range of about $2.5cm$, can be traversed by a sawtooth train of appropriate length. To monitor the position, the laser beam of an interferometeric displacement sensor (PicoScale, by SmarAct) is reflected off of the upstream side of the sapphire, which is gold-coated for efficient reflection. The output of the interferometer is then fed into the same computer generating the sawtooth train, to close the feedback loop.

Although the PI x-y scanning stage is equipped with internal capacitive position sensors, we decided to use the same interferometeric mechanism described above for this stage as well. The reason for this is made clear by Fig. 3.2: due to the added mechanical path length (due to the bracketry described above) separating the zone plate from the internal sensors, the two positions aren't fully coupled. Measuring the zone plate position as close to the zone plate itself as possible ensures more precise positioning.

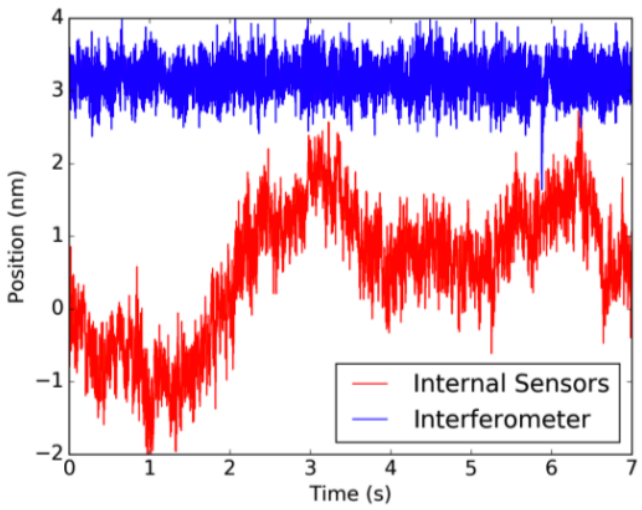

Figure 3.2: Position feedback: internal capacitive sensors of the stage vs. interferometric monitoring close to the zone plate. Here, the x-y scanner is holding position in feedback with the interferometer, as position is measured by both the interferometer and the internal sensors. Previously published in [87].

Fig. 3.3 visualizes the setup described in this section.

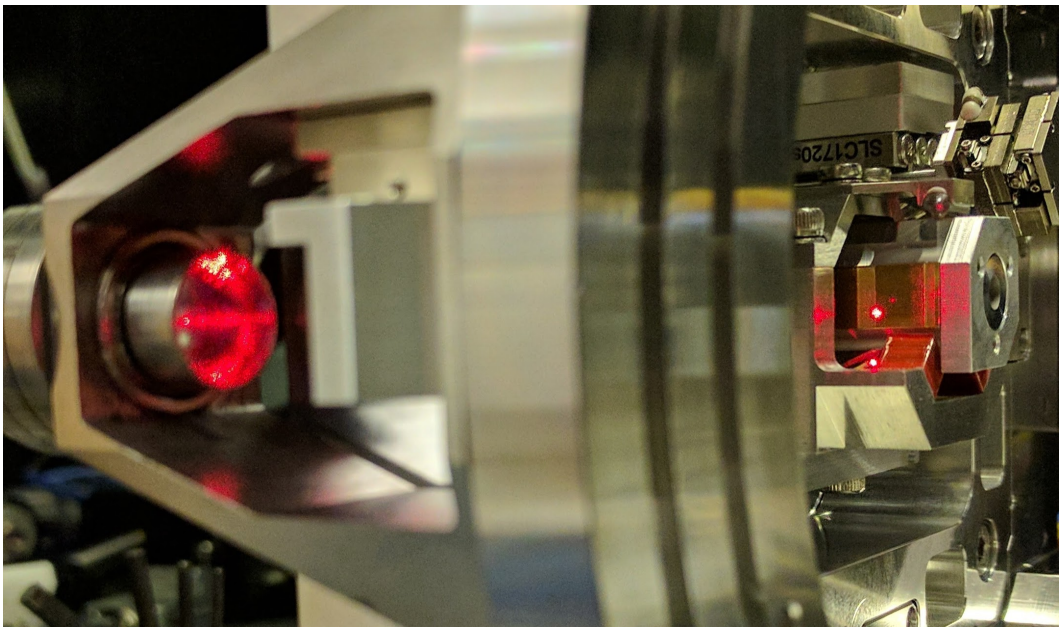

Figure 3.3: Zone plate stages: The red alignment laser reflects off of the gold-coated side of sapphire octagon, at the tip of which the zone plate would be mounted, demonstrating interferometric position measurement, which is fed back to the scanning stage to enable nanometer positioning and scanning. The two forward piezo sheer actuators (in orange) are visible under the sapphire. Towards the top right the motor used for mounting and positioning the OSA is visible, attached to the same bracketry, mounted on the x-y scanner.

3.1.3 Sample Stage

As was mentioned before, a commercial sample stage from an electron microscope (an FEI TEM CompuStage, in this case) was chosen for Nanosurveyor 2. Although a stage (along with the TEM column piece housing the stage) was acquired, little information about the stage was available, an no motion controller. The task was then to map the electrical connections, and route and process them so that the stage could be driven with a typical motion controller (a Newport XPS motion controller, in this case.)

The stage has four axes: x, y, z, α(rotation, for tomography). The electrical connections available from the stage were grouped into five cables. Investigations showed that each axis had a few electrical connections associated with it: for driving the motors, sensing the position (for feedback), and limit switches. The collection of all these signals from all axes were distributed, with no apparent pattern, in the five cable connections. The XPS controller, however, requires all of the signals corresponding to a single axis to be grouped into one cable connection. Therefore, the wires carrying the signals for each axis were identified, isolated, routed, processed when needed (i.e. converting quadrature position signals), and grouped into self-contained axes. Fig. 3.4 illustrates the box engineered to handle this task.

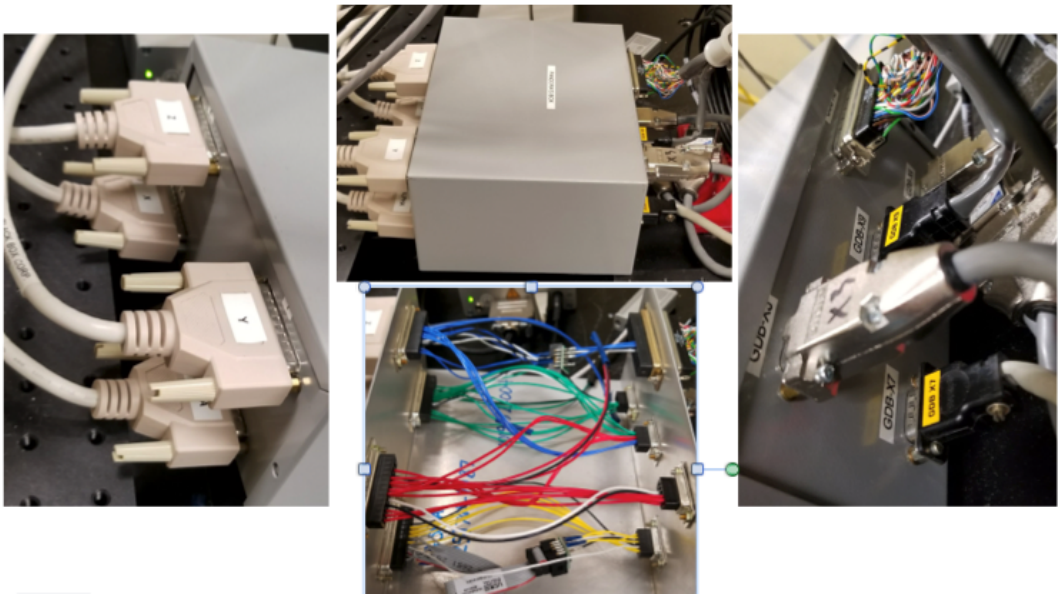

Figure 3.4: Sample stage connections: wires carrying the signals for motors, sensors, and limit switches arbitrarily distributed among five connections, entering the box (right), getting routed and processed (middle), and leaving the box in self-contained individual axes (left) to the motion controller.

3.1.4 The Instrument's Environment

Three additional stability measures were taken in the instrument's environment: to decouple the instrument from ground motion, to passively thermally and acoustically isolate the instrument, and to actively reduce thermal variation.

Support Structure

To isolate the instrument from ground motion (both low frequency vibrations and displacements: the ALS floor is 'soft' and susceptible to small displacement due to the movement of people and equipment) a large, heavy support structure was utilized. The terminal beamline elements (various beam-shaping slits, shutter, and diagnostics) were mounted on the same structure, so as to couple their motion to that of the microscope. The instrument itself is further separated from the structure via a secondary slab, resting on elastic pods attached on top of the support structure. This combination proved effective: gentle knocks on the slab produce vibrations clearly visible on the interferometer readout, whereas even strong bumping of the support structure produces no visible effect.

Enclosure

An enclosure was built around the instrument for passive acoustic isolation from the noisy ALS environment, and also to provide passive thermal isolation. The enclosure includes most of the support structure as well. There is enough room provided for final sample preparation and initiation of the experiment by the user(s); but the intent is for the room to be evacuated once the sample is inserted. The instrument is controlled remotely from a nearby room. Fig. 3.5 shows the instrument inside the enclosure.

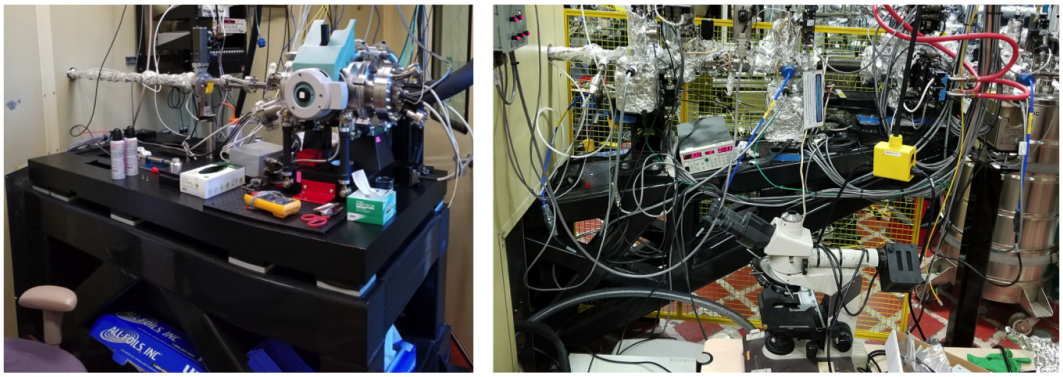

Figure 3.5: The instrument situated on the support structure within the enclosure (left) and the portion of the support structure on which terminal beamline components (slits, diagnostics, etc) are mounted, upstream of the enclosure (right).

Active Thermal Control

To further improve upon the passive thermal isolation enabled by the enclosure, a heater-chiller combination was deployed. A temperature sensor, located immediately next to the instrument, is used in feedback with the heater-chiller to keep the temperature steady.

3.2 Performance

Here we characterize the performance of Nanosurveyor 2 as described above. All the measurements discussed below were taken in real operating conditions, with the microscope installed at the beamline, and the various sources of noise (vacuum pumps, etc) active.

3.2.1 Vibrational Stability

Zone plate position data were recorded for both x and y axes using the interferometer and analyzed for vibration. Fig. 3.6 shows the spectra. The zero-mean rms (standard deviation) were calculated to be $0.5nm$ for both axes.

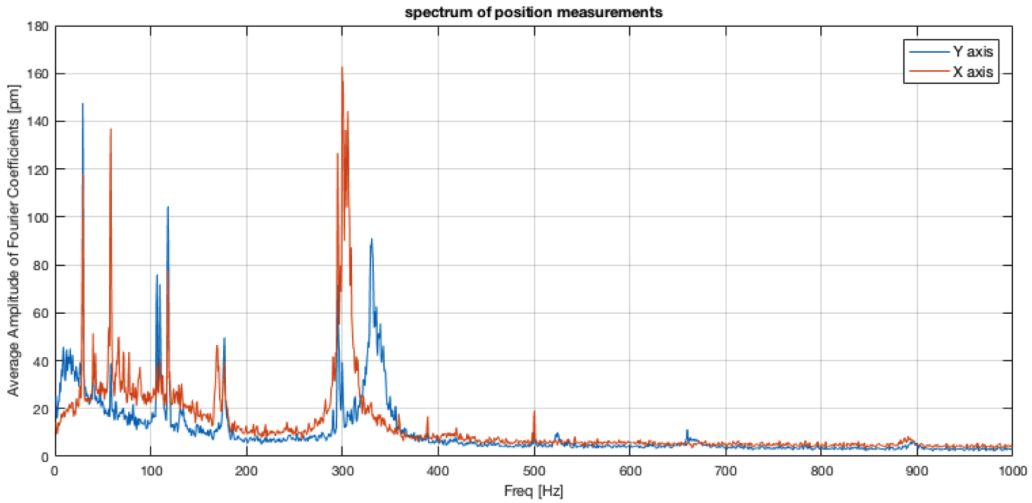

Figure 3.6: Zone plate vibrations in x and y as measured by the interferometer

We attribute the broad peaks around 300Hz to mechanical resonances of the system, whereas the sharp peaks at lower frequencies are due to environmental sources. Lower resonance frequencies, coinciding with the environmental sources of vibration, would have resulted in amplification, and the vibration rms would have been higher.

3.2.2 Temperature Stability

With the enclosure isolating the instrument from the environment, and active thermal control implemented as described in the previous section, temperatures were recorded over several hours (a ptychography scan can take multiple hours, depending on the area of the region of interest.) by the same temperature sensor used in feedback. This is plotted in Fig. 3.7. Variations over many hours remain within about 0.1 degrees Celsius.

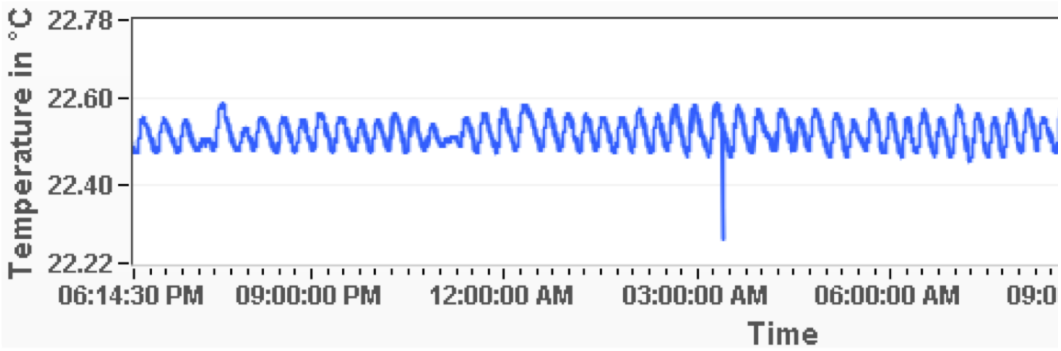

Figure 3.7: Temperature as measured by a sensor located immediately adjacent to the microscope

3.2.3 Drift

To measure system-wide drift, a sample was imaged in STXM mode repeatedly for more than an hour. (STXM was used for two reasons: much faster scan times, and sample position not subject to reconstruction but directly measured.) The images were then cross-correlated to measure relative motion. Results for both axes are plotted in Fig. 3.8, showing steady drift over a span of 72 minutes, for a total of $140nm$ in x and about $195nm$ in y, corresponding to an average drift of $2-3nm$ per minute.

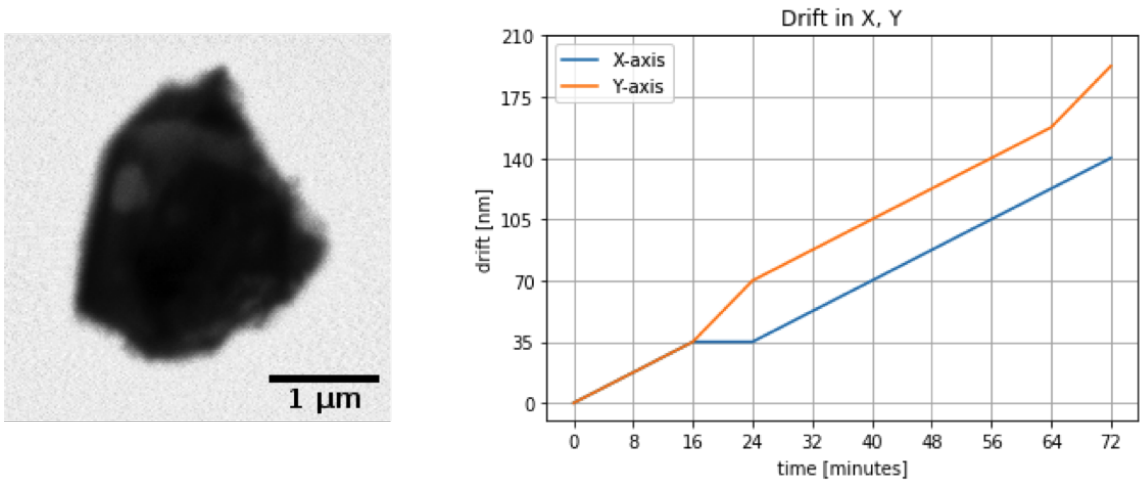

Figure 3.8: System-wide drift as measured by repeatedly imaging a sample (left) for more than an hour, and cross-correlating to find relative drift (right).

3.2.4 Resolution Target Analysis

To characterize the resolution of the system, a binary pseudo-random multilayer resolution target (similar to [88]) was used, fabricated by aBeam Technologies, Inc. The target is a pattern of stripes of $200nm$ thickness and pseudo-random widths, composed of WSi2 and Si2 layers with fundamental layer width of $1.5nm$. (See [89] for more on a similar resolution target.) This sample was imaged at $1000eV$ with a $45nm$ zone plate in dual exposure mode at $200ms$ and $15ms$ to increase dynamic range. Data was reconstructed using SHARP [73]. Fig. 3.9 shows the magnitude and phase of the reconstruction. They are 2391x90 pixels, reconstructed at a pixel size of $3.0nm$ (which was the maximum allowed by the numerical aperture.)

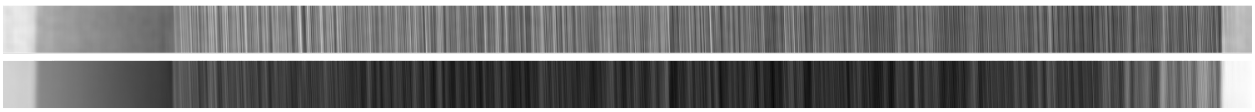

Figure 3.9: Magnitude (top) and phase (bottom) of the reconstructed resolution target

The magnitude of the reconstruction was then used as input to the resolution analysis software corresponding to the resolution target, pSpectra^{TM}, provided by aBeam Technologies, Inc. The software corrects the image for rotation and any perceived distortions, then compares its PSD (power spectral density) against that of the binary pattern used to generate and fabricate the resolution target. The PSD in the orthogonal (vertical) direction is used to characterize noise. Resolution can then be viewed as the highest spatial frequency at which the PSD of the image stays above the noise. (See, for example, [88, 89, 90] for related background and examples of the use of the software.) Fig. 3.10 shows the results. The image PSD stays above the noise level for all spatial frequencies, indicating better than 3nm half-period resolution for the instrument. To our knowledge, this is the highest resolution achieved by a photon-based microscope.

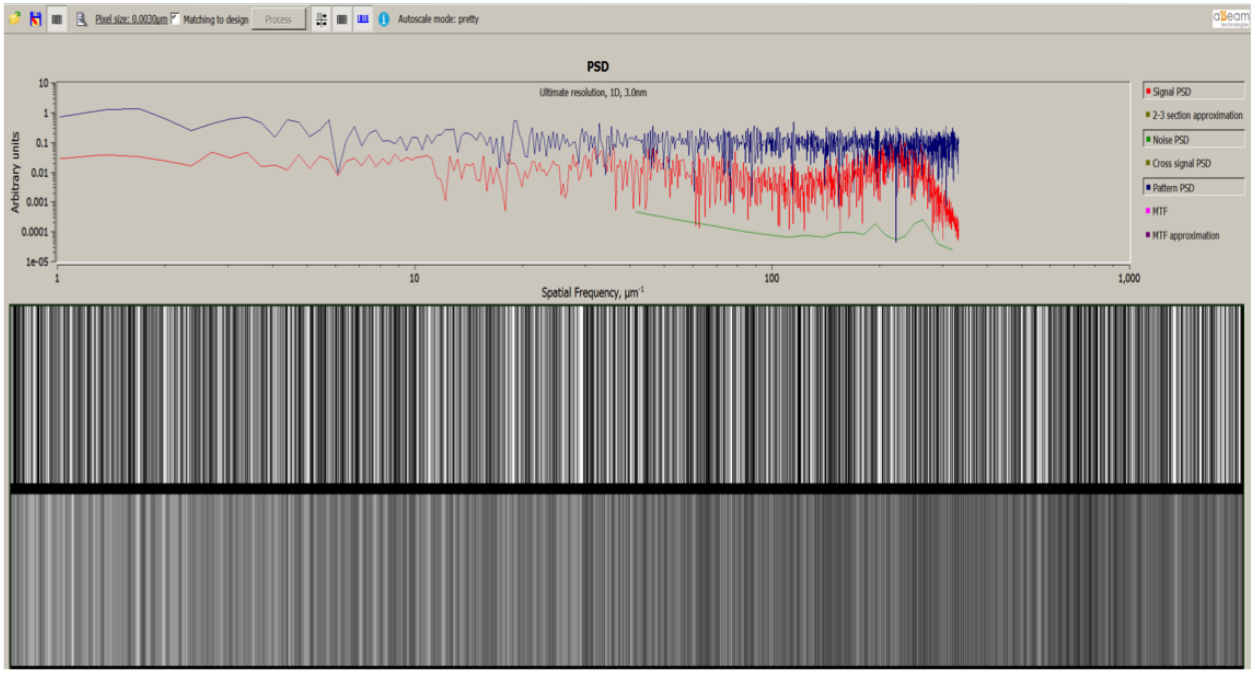

Figure 3.10: A screenshot of pSpectra^{TM}. The PSD of the original pattern is in blue, the PSD of the sample is in red, and the PSD of noise (calculated in the orthogonal direction, here vertical) is in green. The top pattern is the original binary pattern used as 'ground truth'; the bottom pattern is the corrected input image, in this case the magnitude of the reconstruction, matched to the original pattern.

The diffraction patterns collected during the ptychography scan showed scattering to the edges of the numerical aperture. While this suggests that increasing the NA (e.g. by moving the detector closer to the sample) and optimizing exposure times would potentially increase the resolution, it should be kept in mind that resolution is a highly sample dependent concept. Most real-world samples do not scatter this much under practical exposure times (or without suffering from beam damage.) The point of this resolution target analysis, with a 'sample' engineered to scatter to high angles, is to show that given the right sample, the instrument is so stable as to enable high-resolution imaging at close to the wavelength.

3.3 Applications

Nanosurveyor 2 incorporates a sample stage compatible with commercial TEM sample holders, including operando electrochemistry holders (one set of such holders, from Hummingbird Scientific, is already available to users) and double-tilt holders, enabling a host of in-situ experiments with 2 angular degrees of freedom.

The stage is also cryo-compatible, and a cryogenic sample holder is undergoing commissioning, to mitigate beam damage and enable higher resolution imaging of soft matter and biological samples.

The undulator source at the COSMIC beamline also allows full polarization control, enabling magnetism as a contrast mechanism in ptychographic microscopy.

In the next chapter, we discuss spectro-microscopy by a combination of STXM and ptychography.

Chapter 4

Spectromicroscopy by Combining STXM and Ptychography

We saw in Chapter 1 that, in addition to wavelength, x-ray interaction with matter depends on the atomic structure factor in both absorption and phase. This results in unique signatures for different chemical species. X-ray Absorption Spectroscopy (XAS) involves the study of the absorption spectra of materials. (See [91] for details on XAS.) Reference spectra from known chemical species can then be combined with microscopy, by fitting each pixel in multiple images of a sample acquired at a range of energies to these reference spectra, to produce a map of chemicals present in a sample (See e.g. [92] for a review of spectromicroscopy.).

But what if we do not have reference spectra for the particular chemical species we would like to search for? As Lerotic et al demonstrated in 2004 [93], it is possible to apply Principal Component Analysis (PCA) to quantitatively separate the sample into multiple contributors with different chemistry, even though the lack of reference spectra will prevent this approach from establishing a clear one-to-one correspondence between the principal components and known chemistry and further interpretation will be required.

Ptychography has enabled the production of chemical maps at even higher resolutions than possible before, in both 2D and 3D (we have mentioned examples of these in previous chapters, e.g. [10] and [78].) But this typically comes at a high cost: each ptychography scan takes much longer to complete compared to a lower resolution STXM scan of the same field of view, and imparts a higher radiation dose on the sample. Attempting ptychography at tens of x-ray energies, as would typically be required for spectromicroscopy, multiplies that time differential. This is particularly problematic and impractical for large fields of view and for in-situ studies. Here, we investigate a method to speed up spectromicroscopy at high chemical and spatial resolution by extracting chemical information from STXM images at tens of energies, and using this information to analyze ptychography data acquired at only a few energies.

The Sample

Our sample for this investigation is NCA (lithium nickel cobalt aluminum oxide), a material used as cathode in experimental Li-ion batteries. (See [94] for a review of NCA and other Li-ion battery materials.) Although Lithium's cross section of interaction with x-rays is too small and its absorption edge is outside the soft x-ray regime, its presence in the cathode (and thus the charge state of the battery) could be inferred through Nickel's oxidation state, which is reflected in the absorption spectra around the Nickel L-edge. We can then infer the charge state of the battery material from variations in the oxidation state of Nickel.

The Experiment

An energy scan was first conducted to probe the Nickel L-edge at Nanosurveyor 2, installed at the ALS COSMIC beamline (7.0.1.2), showing the Lα and Lβ edges roughly around 855eV and 870eV, respectively. (This suggests a beamline offset of a few eV from the tabulated reference values [95].) Microscopy data was then collected in the form of two stacks: 1-a STXM stack at 72 energies ranging from 850eV to 885eV, at increments of 0.25eV for intervals [854,860]eV and [870,876]eV, and at increments of 1eV for the rest, and, 2-a ptychography stack at energies 854.25, 854.5, 854.74, 855, 855.25, 857, 858.25, 868, 874.25, all in eV. A 45nm zone plate was used in both STXM and ptychography mode

Analysis

Spectromicroscopic analysis of the data can be divided into two parts: 1-extracting chemical information from the STXM stack, and, 2-using this information to visualize chemistry at high resolution using the ptychography stack.

We will start with step 1. As we change the x-ray energy to conduct 72 STXM scans, the zone plate focal distance changes (the zone plate is a chromatic optic, as discussed in Chapter 1.) Any imperfection in the z-axis motion of the zone plate stage would result in translating the beam on the sample. Thus, we need to first rigidly align the stack. This is accomplished by first aligning the second image to the first image, then iteratively aligning successive images to the mean of the aligned images. The alignment is further refined by affine-registration of individual frames to the mean of the aligned stack. Fig. 4.1 shows the mean of the aligned stack, as well as two individual STXM images before and after the Ni Lα edge.

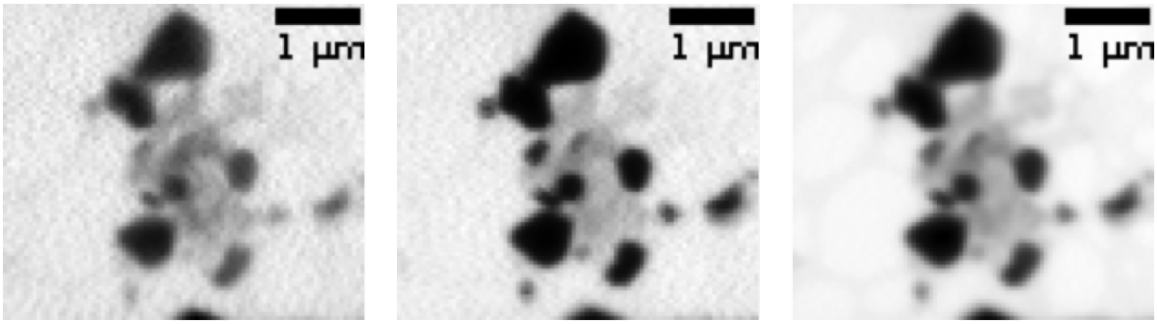

Figure 4.1: STXM images of the NCA sample at 850eV (left), 857.5eV (center), and the mean of the aligned STXM stack (right). Note the change in contrast due to change in energy.

Next, the optical density of the STXM frames is calculated (with optical density defined as $OD = -ln\left(\frac{I_T}{I_0}\right)$, with I_T denoting transmitted intensity and I_0 denoting background intensity.) We used the 98th percentile brightness in the stack average as the threshold for background, and set any negative OD values (which would result from noise in the background) to zero.

What conveys information about the chemistry of the sample is not the full optical density at each energy, but the *change* in optical density with changing x-ray energy. The remainder, constant offset can be ascribed to sample thickness. To remove pre-edge thickness effects, therefore, we subtract the pre-edge optical density of the image at the lowest energy from the entire stack. We then perform PCA on this stack. Fig. 4.2 shows the scree plot, visualizing the amount of variation in the data explained by each principal component.

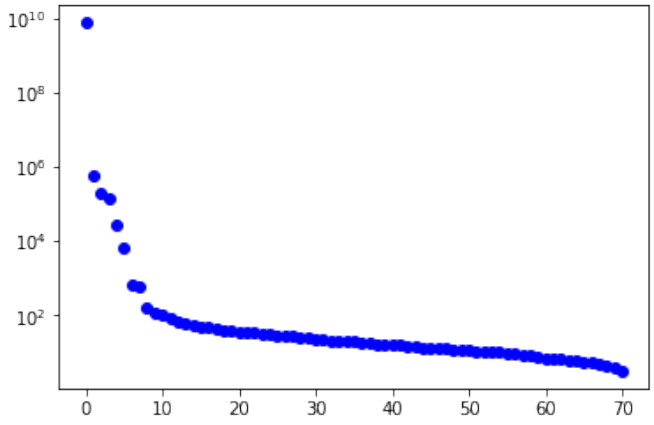

Figure 4.2: the scree plot of PCA on the STXM optical density stack

The top four components are then used for k-means clustering. Fig. 4.3 shows the clusters, as well as the spectra extracted by averaging the optical density of each cluster.

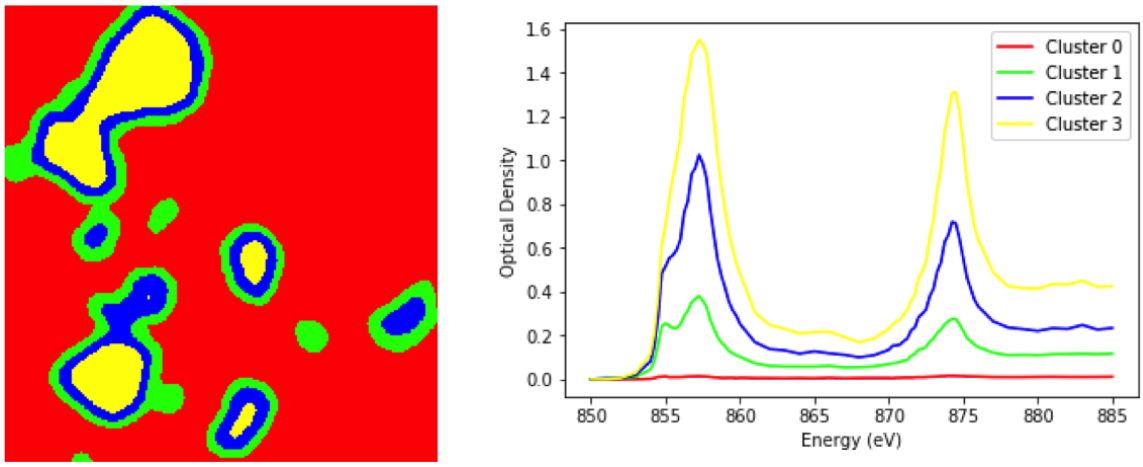

Figure 4.3: k-means clustering, and the spectra extracted from these clusters

It should be noted that these spectra, obtained from PCA and k-means clustering, do not necessarily correspond to any pure/pristine chemistry; they represent abstract variations in the data with changing x-ray energy, which contains chemical information, and requires further interpretation. Here, we could interpret the clusters as different charge states of the battery material, though there might be other information present as well, such as possible saturation in the thicker areas of the sample.

Cluster 0 is clearly capturing the background, and includes a lot of noise as is visible from the normalized spectra. But clusters 1, 2, and 3 seem to represent changing chemistry of the battery material, as the shifting peaks in the spectra around the L3 edge correspond to different oxidation states of Ni. We will use the spectra from clusters 1, 2, and 3 to fit the ptychography optical density stack.

We start by first aligning the ptychography stack, similarly to what was described for the STXM stack. Fig. 4.4 shows the mean of the aligned stack, as well as images (magnitudes of reconstruction) at two distinct energies.

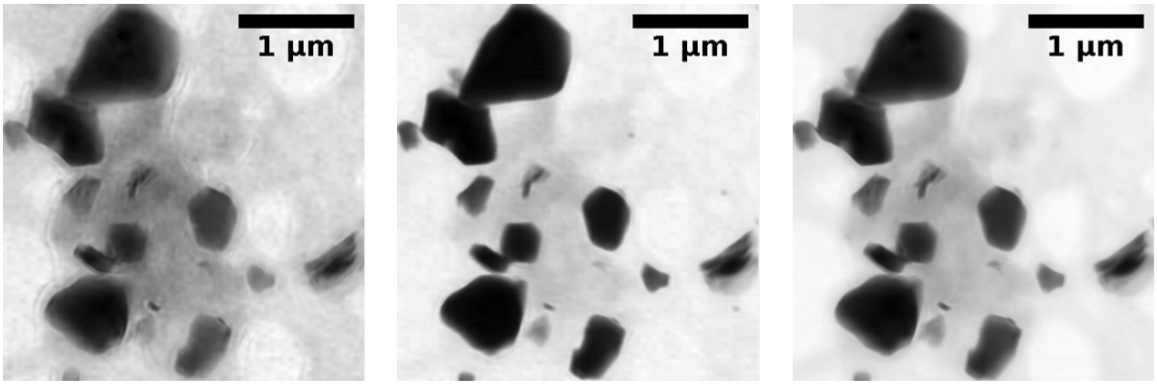

Figure 4.4: ptychography images (in magnitude) of the sample at 854.25eV (left) and 857eV(center), and the mean of the ptychography stack (right)

The optical densities are then calculated for these ptychography images, similarly to what was described in the case of the STXM images. Fig. 4.5 shows the optical densities for images shown in Fig. 4.4.

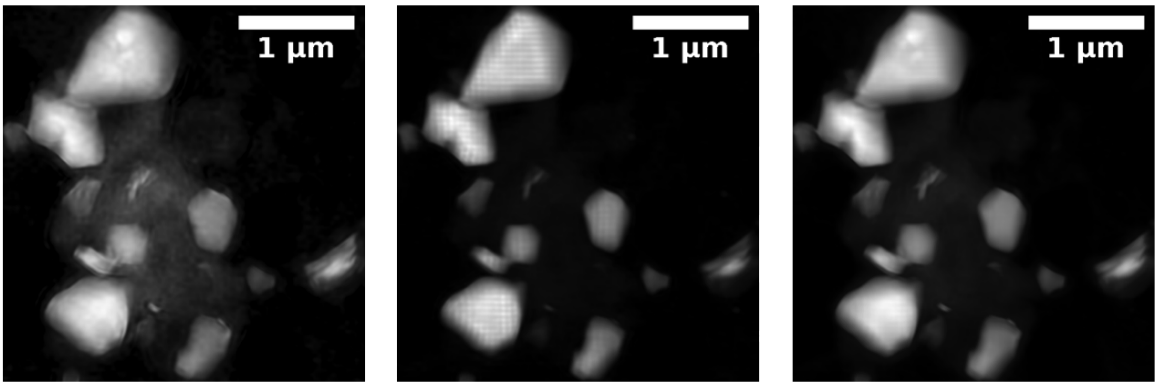

Figure 4.5: optical densities of ptychography images shown in the previous figure: 854.25eV (left) and 857eV(center), and the mean of the optical density stack (right)

There's one last step before the stack is ready for fitting to spectra: we need to subtract the pre-edge from the optical density stack in order to eliminate pre-edge thickness effects, similar to what we did in the case of STXM optical densities. In this case, we have not recorded ptychography images at a low enough energy to be quite in the flat spectral region of pre-edge. The lowest energy at which we have a ptychography image is 845.25eV, which is at a point where the first peak is just beginning to emerge. Although it is not ideal, we will use this energy for pre-edge subtraction.

We're now ready to fit the ptychography optical density stack to the normalized spectra extracted from STXM. Since only non-negative amounts of each chemical phase make physical sense, we will use Non-negative Least Squares (NNLS) optimization to do the fitting.

The results for the 3 components are shown in Fig. 4.6. Each image corresponds to the spectra from one of the clusters. The image value at each pixel is the coefficient of the spectra corresponding to that image.

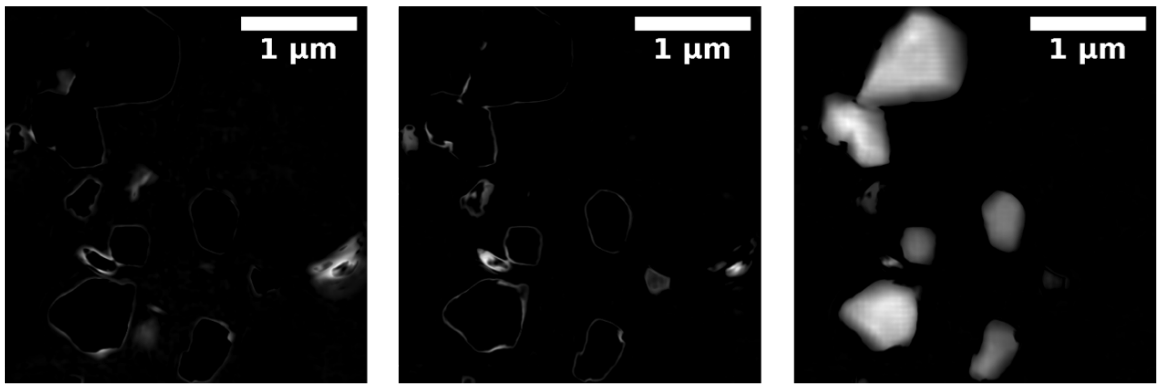

Figure 4.6: The results of NNLS fitting to clusters 1 (left), 2 (center), and 3 (right)

To better visualize the fitting, we create a 'chemical map' by creating a composite RGB image using these three fit components, as visualized in Fig. 4.7. For comparison, the results of the same analysis applied to the STXM optical density stack is also included.

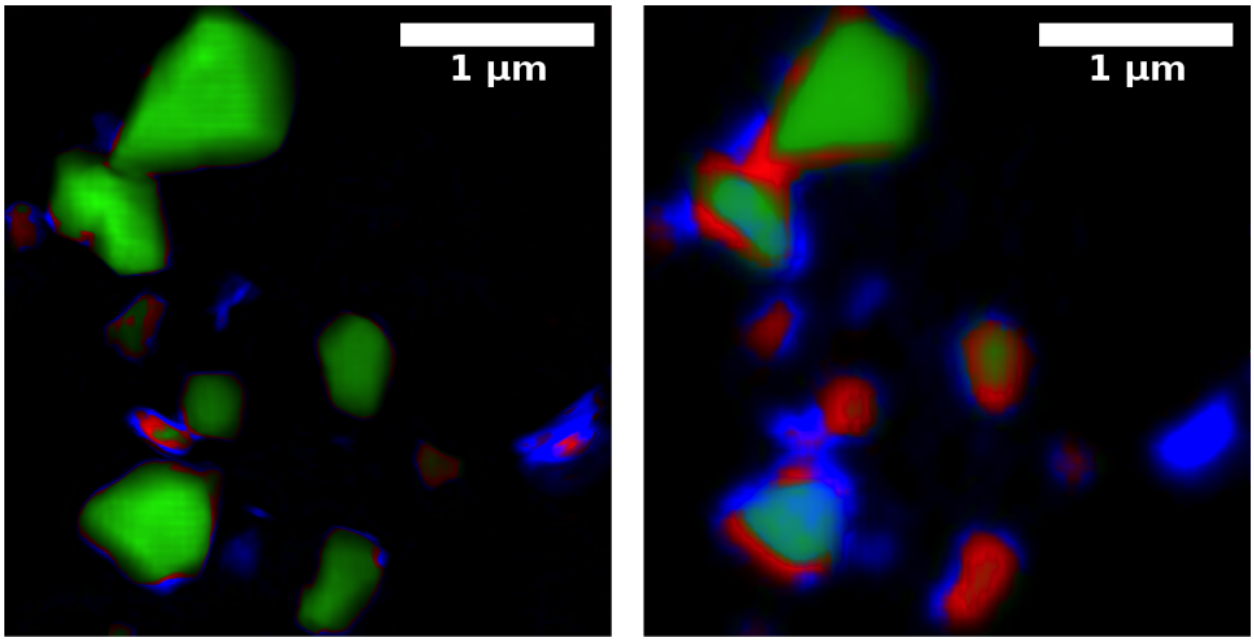

Figure 4.7: chemical map of the sample, obtained by creating an RGB map composed of the ptychography optical density fits to the spectra extracted from STXM clusters (left). Similarly produced STXM chemical map is on the right.

The general pattern of charge-discharge happening at interfaces can be seen in both images; but the ptychography chemical map is clearly more detailed and provides chemical information at higher resolution, as would be expected due to ptychography's generally higher spatial resolution compared to STXM. This is especially helpful at the interface and for smaller particles, where there are chemical variations on a smaller scale.

Although the two maps largely agree qualitatively, there are some disagreements as well, notably in the particle in the bottom-center of the field of view. This particle has mapped largely to the spectra from cluster 3 in ptychography, but cluster 2 in the STXM chemical map. To further investigate the accuracy of this method, results should be compared with a ptychography chemical map obtained from a full energy stack.

High-resolution chemical maps obtained using this method take significantly less time compared to obtaining a full ptychography energy stack. This will facilitate in-situ studies, where multiple chemical maps at different stages of an experiment (battery particles undergoing charge-discharge, for example) are needed.

Chapter 5

Scanning Improvements and Future Work

Scanning is an integral and important aspect of ptychography. Traditionally, the simplest way to scan the beam has been in a raster-scan grid pattern. Doing this with a $45nm$ zone plate, with a step size of $30nm$, would result in roughly a thousand scan positions (and diffraction patterns) per square micron of the field of view. This is expensive in total exposure time and data, and in scan overhead time. Here, we investigate ways to reduce these costs while only minimally affecting the final results.

5.1 Step-Dependent PID Control in Zoneplate Scanning

As was mentioned in Chapter 3, laser interferometric measurement of the zone plate position is used in feedback with the piezo motor to enable nanometer positioning of the zone plate during scanning. The feedback loop is closed by the piezo motion controller (in our case, an nPoint LC400 series controller). The feedback loop is configured with 3 parameters: Proportional, Integral, and Derivative (PID). (PID control has a well-established history, and introductory literature is readily accessible online. More in-depth resources include [96, 97].) Here, we describe a simple yet effective technique to improve scanning speed and stability by adjusting PID parameters during a scan.

In general, the goal for tuning the PID parameters for the scanning stage is to enable the stage to reach the target position in the shortest time possible, and to stay stably in place after reaching the target. The difficulty is that there is a trade-off between the speed and the stability: tuning the stage too aggressively can get the stage to reach the target very fast, but it will then oscillate around the target before settling; and tuning for perfect stability at the target position increases the time it takes to get to the target. Tuning the stage just right involves finding that narrow acceptable band of parameters where the stage gets to the target position just fast enough and remains there just stable enough.

In a stage with a large enough range of possible steps, such as our zone plate scanning stage with a range of desirable step sizes from tens of nanometers to tens of microns, there is a second difficulty: the response of the stage to the PID parameters varies with step size as well, with more aggressive tuning being optimal for smaller step sizes. This is demonstrated in Fig. 5.1 by first properly tuning the stage for step sizes of $50nm$ and $25\mu m$, noting the similarity in timing, then reversing the tuning parameters and comparing the results.

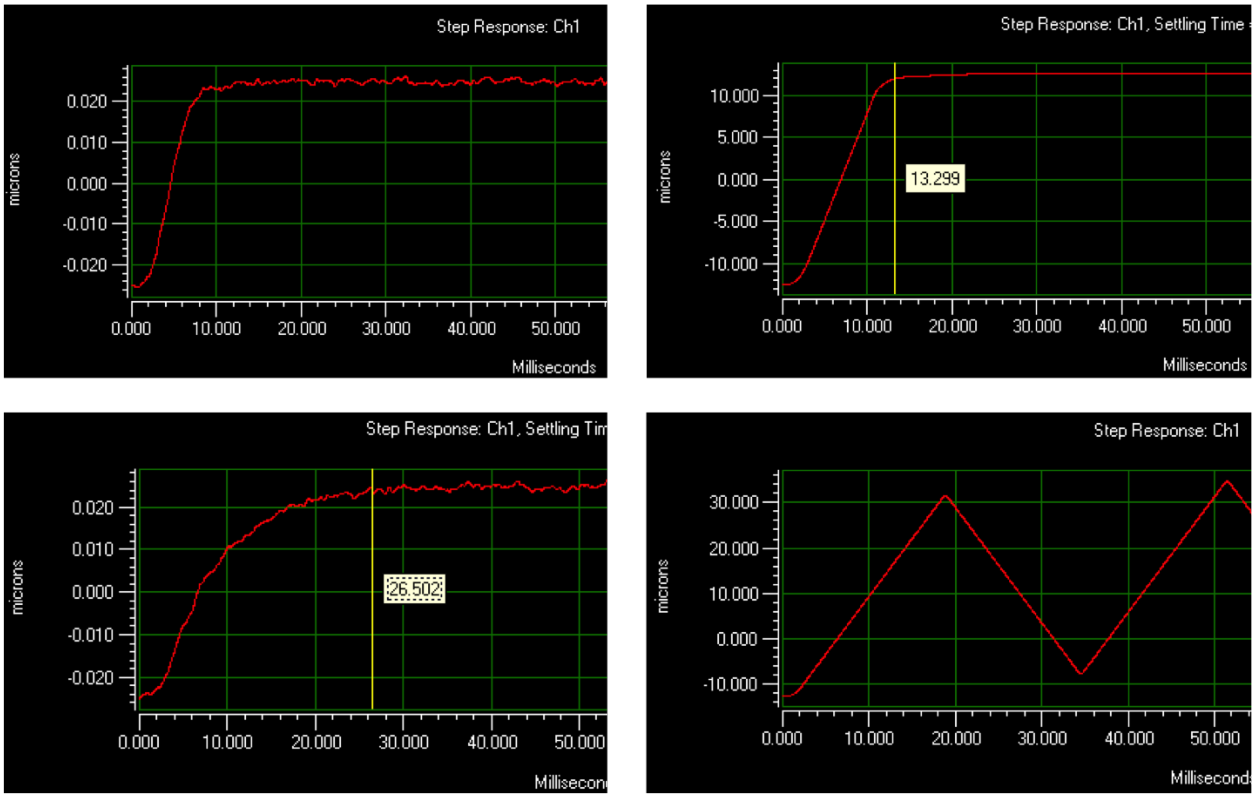

Figure 5.1: Step-size dependence of piezo stage PID tuning: The zone plate scanning stage is first properly tuned for step sizes of $50nm$ (top left) and $25\mu m$ (top right), showing comparable settling times of $8ms$ and $13ms$ when individually optimally tuned. The tuning parameters are then reversed for the two step sizes, resulting in increased settling time of $26.5ms$ for the $50nm$ step (bottom left) and wild oscillations for the $25\mu m$ step.

The typical approach then would be to compromise and accept a middle ground: tune the stage less aggressively than optimal for short steps, accepting the loss of a few milliseconds per step, while also being more aggressive than optimal for the longer steps, resulting in oscillations for possibly tens of milliseconds, which again add to the overhead.

To eliminate this extra overhead, the stage was first optimally tuned for a range of different step sizes and the optimal PID parameters were recorded in a look-up table. A scanning script was then developed in python to adjust the nPoint controller's PID parameters on-

the-fly depending on the step size of the upcoming step. Fig. 5.2 shows the results during a raster scan.

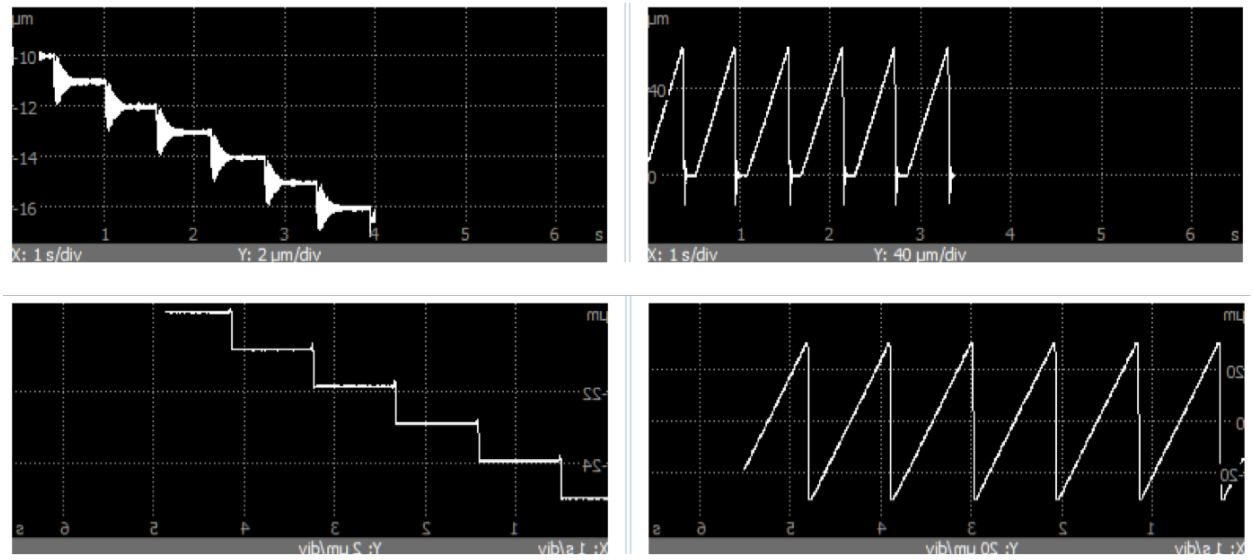

Figure 5.2: Raster scanning the stage with constant PID parameters chosen in between those optimal for small and large step sizes as a compromise (top row) and optimal step-dependent PID parameters adjusted in real-time (bottom row). The two plots in each row show the x and y axes during a raster scan.

The result is that steps of different sizes are all optimized to reach the destination in the shortest time possible, and to stay in place without oscillating, removing the need for additional settling time, which would otherwise add to overhead. This approach can save valuable scan overhead time in a ptychography scan. This is increasing important as brighter sources are developed, increasing the ratio of the scan overhead time to actual exposure time.

5.2 Selective Subsampling of Diffraction Patterns in Ptychography

As was mentioned in our review of ptychography in section 2.3, illumination overlap between neighboring scan positions is at the core of ptychography. In the past, studies have been done investigating the amount of overlap between neighboring scan positions. (e.g. see [58].) Here, we investigate the effect of skipping some scan positions and collecting less data than would usually be collected.

The sample used for this investigation is a collection of gold nanoparticles, $50nm$ in diameter, deposited on a silicon nitride membrane. Data was collected on the Nanosurveyor 1 instrument at the ALS beamline 5.3.2.1, with a $90nm$ zone plate, and reconstructed using SHARP. Fourier Ring Correlation (FRC) analysis [98] was used to characterize resolution. Fig. 5.3 shows the results, when data is acquired as usual with a raster scan with a standard step size of $75nm$, and all scan positions are included.

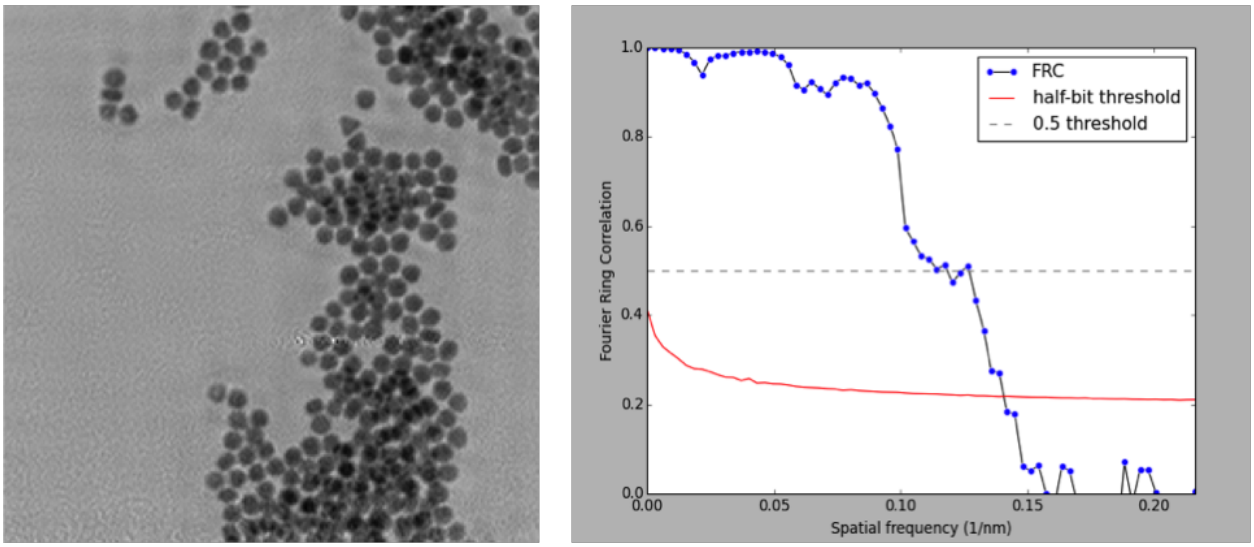

Figure 5.3: magnitude of the reconstruction of a ptychography scan of a collection of 50nm gold nanoparticles (left), and the FRC resolution analysis (right). The field of view is 1.3x1.3μm^2. The FRC curve meets the half-bit threshold at a spatial frequency of $0.133nm^{-1}$, indicating a resolution of $7.5nm$.

FRC analysis indicates a resolution of 7.5nm with the full set of diffraction patterns. Next, we use the same data, but omit various diffraction patterns from the full set. We look for the effect of this subsampling on both the analyzed resolution and the overall quality of the reconstruction. Various patterns and percentages were used in selection of diffraction patterns. We note our observations below.

This particular sample showed a good degree of resilience to omission of up to 50% of diffraction patterns. Fig. 5.4 shows the results with a regular, periodic pattern used to select the diffraction patterns.

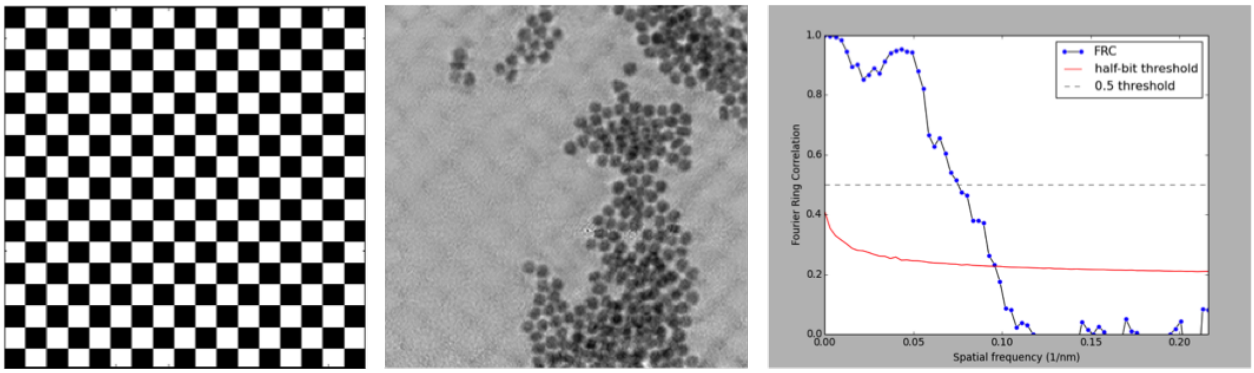

Figure 5.4: magnitude of the reconstruction of a ptychography scan of a collection of 50nm gold nanoparticles (center), reconstructed using a subset of the diffraction patterns as visualized by the scheme on the left (dark locations correspond to omitted diffraction patterns), and the FRC resolution analysis (right). The FRC curve meets the half-bit threshold at a spatial frequency of $0.09nm^{-1}$, indicating a resolution of $11nm$.

Perhaps the most noticeable feature in this reconstruction is that the pattern used to select the diffraction patterns seems to be imprinted as a reconstruction artifact. To get around this, we break the symmetry by randomizing the pattern, still omitting 50% of the diffraction patterns. Fig. 5.5 shows the results.

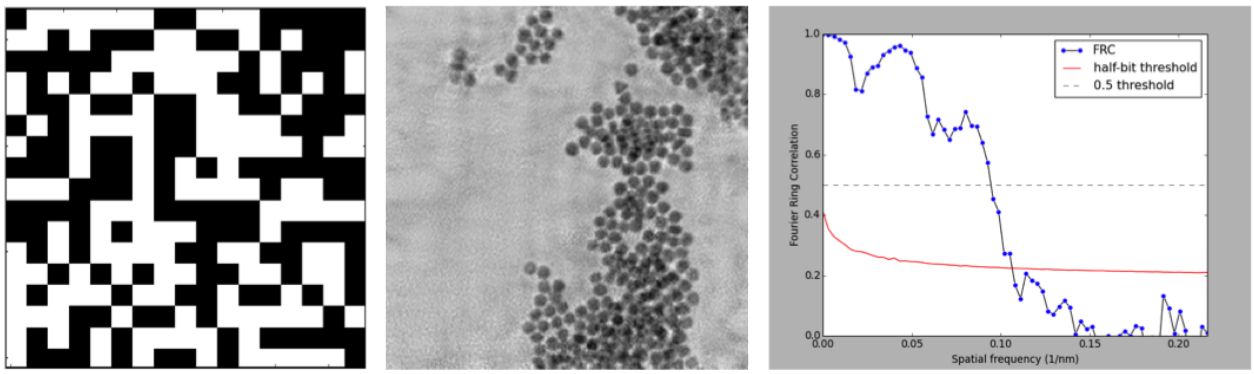

Figure 5.5: magnitude of the reconstruction of a ptychography scan of a collection of 50nm gold nanoparticles (center), reconstructed using a subset of the diffraction patterns as visualized by the scheme on the left (dark locations correspond to omitted diffraction patterns), and the FRC resolution analysis (right). The FRC curve meets the half-bit threshold at a spatial frequency of $0.1nm^{-1}$, indicating a resolution of $10nm$.

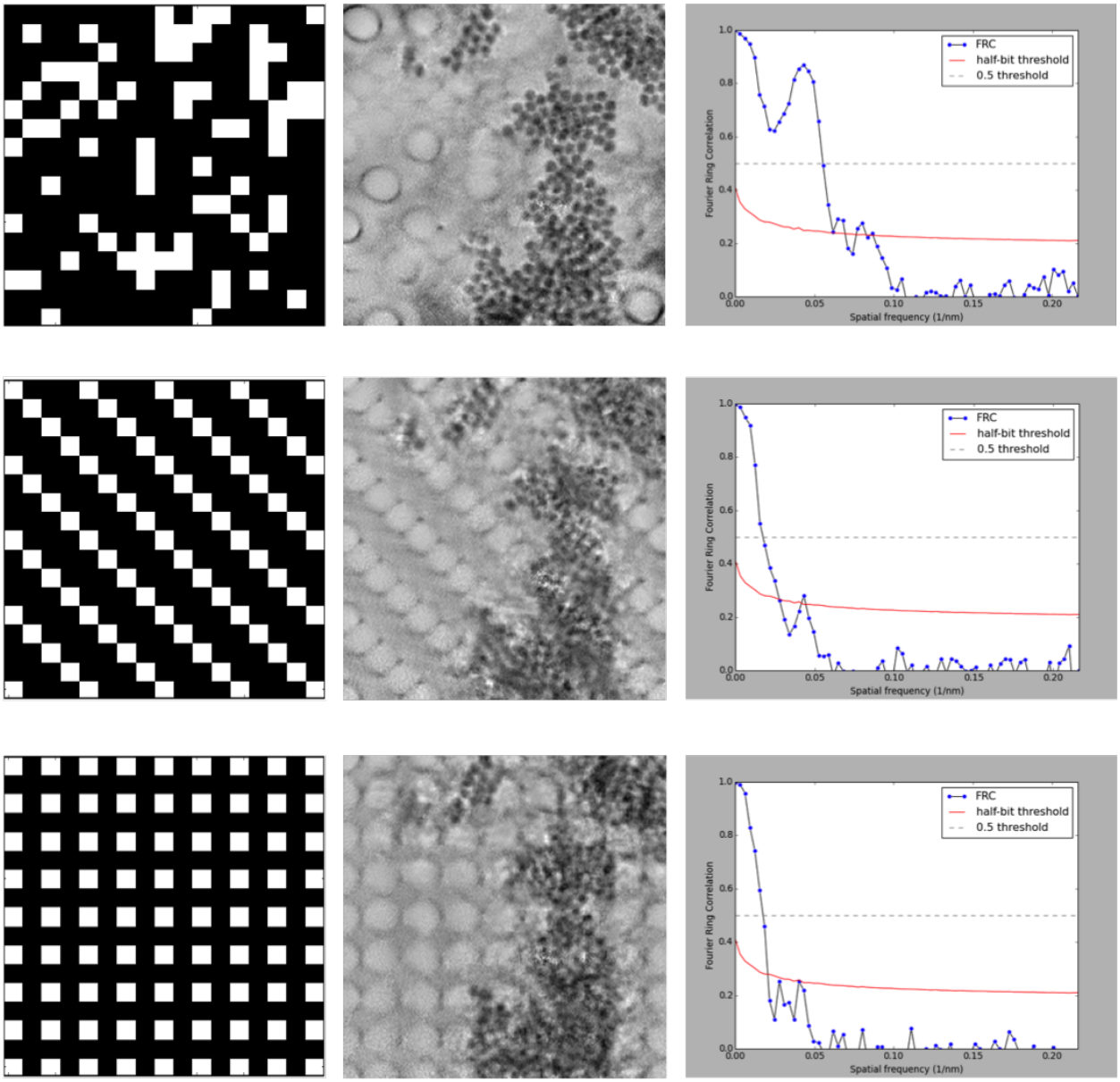

Figure 5.6: magnitudes of reconstruction of ptychography scans of a collection of 50nm gold nanoparticles (center column), reconstructed using a 25% subset of the diffraction patterns as visualized by the schemes on the left (dark locations correspond to omitted diffraction patterns), and the FRC resolution analyses (right column). The FRC curves meets the half-bit thresholds at spatial frequencies of $0.058nm^{-1}$, $0.022nm^{-1}$, and $0.019nm^{-1}$ from top to bottom rows, indicating resolutions of 17, 45, and 53 nanometers, respectively.

This experiment was repeated with various other patterns and fractions of diffraction patterns excluded. Fig. 5.6 shows three results with different patterns, each excluding 75%

of the diffraction patterns.

With this particular sample, multiple trials with various random patterns excluding up to half of the diffraction patterns yielded similar results in quality and resolution of the reconstruction for a given exclusion percentage. Excluding more diffraction patterns than half, however, led to results highly dependent on the particular patterns chosen. Nevertheless, random patterns consistently outperformed symmetric or periodic patterns, such as those in the second and third rows of Fig. 5.6. This can partly be explained by thinking about the overlap: with random scan patterns, there will probably be areas of illumination on the sample with nanoparticles present where there are multiple adjacent overlapping diffraction patterns, instead of consistently lower density.

Taking this intuition a step further, future work may include designing optimal non-uniform scan patterns instead of leaving the non-uniformity up to randomness. Various types of non-uniform ptychography scan patterns have already been studied (e.g. by Huang et al in [99]), but with constant density throughout the field of view. Low resolution STXM scans are always the first step in order to identify the region of interest and field of view, leading up to a ptychography scan. The STXM image could be used as *a priori* information, based on which the ptychography scan pattern is designed, with a less dense scan pattern in areas identified as background, and higher scan density in areas of less STXM transmission. To further optimize the pattern, it is conceivable that Machine Learning algorithms can be trained on STXM-ptychography datasets to further adjust scan density based on changes in STXM transmission.

The combination of more efficient scanning of the zone plate stage, discussed in the first part of this chapter, and intelligent adjustment of non-uniform scan density throughout the field of view, will enable faster ptychography scans with reduction in data collection and total radiation dose, while minimally (if at all) affecting the reconstruction quality and resolution.

Chapter 6

Conclusion

The confluence of a host of enabling technologies, including bright, coherent synchrotron facilities, advanced computational imaging algorithms, powerful computers, advanced detectors, and precise instrumentation, have made it possible for ptychography-based x-ray microscopes to emerge as the highest resolution photon-based microscopes in recent years. Developed and operated at modern x-ray synchrotron facilities, these microscopes provide researchers with a wealth of information about their samples, including phase information (in addition to absorption), chemical specificity, and bulk information up to microns deep, thanks to large attenuation lengths of x-rays. This has enabled new science, such as study of charge-discharge behavior of battery materials. This dissertation presented new developments in instrumentation and analysis at the Advanced Light Source synchrotron in Berkeley, advancing the state of x-ray ptychography, and explored ideas to further develop the field in the coming years, in preparation for the arrival of Diffraction Limited Storage Rings [100].

After reviewing x-ray interaction with matter and x-ray microscopy in Chapter 1 and x-ray CDI in Chapter 2, we introduced the Nanosurveyor 2 instrument in Chapter 3. Design and integration of various components were described, including the zone plate scanning stage with precise nanometer positioning enabled by interferometric feedback, and the sample stage compatible with commercial in-situ and cryogenic TEM sample holders to facilitate operando experiments and multimodal imaging. The microscope environment was described, including a base to isolate from ground movements and vibrations, and passive and active thermal isolation, limiting temperature variations at the microscope to 0.1 degrees Celsius over the span of hours. Finally, the performance of the microscope was characterized, demonstrating vibration rms of half a nanometer in both transverse dimensions at the zone plate and system-wide drift of two nanometers per minute, enabling spatial resolution of better than three nanometers with a fabricated resolution test target.

Chemical specificity is one of the strengths of x-ray microscopy, enabling the production of chemical maps by analyzing multiple images at a range of x-ray energies spanning an absorption edge. Although routine with STXM, spectromicroscopy data collection in ptychography mode can take many hours or days. In Chapter 4, we demonstrated a new way of speeding up this process by combining STXM and ptychography. A full STXM energy stack

is first collected at typical, fine, x-ray energy increments. The chemical spectra are then extracted from this stack by PCA and clustering. The magnitudes of ptychography images, collected at only a few energies, are then fit to these extracted spectra by Non-Negative Least Squares optimization, resulting in a chemical map at high spatial resolution. This approach was demonstrated with NCA, an experimental battery material, in a mixed charge state. The chemical phases were mapped using the three extracted spectra corresponding to the top three principal components. The final chemical map, resulting from fitting the ptychography magnitudes to the spectra, visualize the chemistry at higher spatial resolution, more clearly separating the chemical phases compared to the STXM chemical map.

Finally, in Chapter 5, we addressed scanning and data collection in ptychography. The PID parameters used to establish interferometric feedback with the piezo stage are only optimal for a range of step sizes. Typical compromises in tuning to make the stage usable for a vast range of step sizes increases scanning overhead. We showed that by adjusting PID parameters on the fly based on the upcoming step size, we could reduce this overhead. On the data collection side, we explored varying the scan densities throughout the field of view, and compared results, judged by reconstruction quality and resolution. On our test sample of a collection of gold nanoparticles, we found it possible to significantly reduce data collection while only minimally affecting results. Randomly generated scan patterns proved more effective that regular, periodic patterns with uniform density. A priori information, such as low resolution STXM scans typically performed as a precursor to ptychography, could be used in the future to more intelligently design scan patterns, reducing data collection times and total radiation dose, while only minimally affecting results.

The longstanding promise of Diffraction Limited Storage Ring facilities is finally starting to be realized around the world. At Berkeley, the Advanced Light Source Upgrade project (ALS-U) is well underway. This will result in an increase in coherent brightness by a factor of tens to hundreds, depending on energy and beamline. For x-ray ptychography, this will enable much shorter exposure times per diffraction pattern if spatial resolutions at the current levels are desired, although mechanical zone plate scanning and CCD readout time will prevent the total imaging time to be shortened by the same factor of tens to hundreds. Addressing these bottlenecks will become very important; and the techniques discussed in Chapter 5 will prove helpful. Additionally, increasing the illumination spot size on the sample could further reduce the scanning overhead by requiring fewer scan positions, provided that the CCD meets the oversampling requirements. (This could be combined with structured illumination, e.g. [101].) The resulting increase in imaging speed will not only increase the overall scientific throughput, but will improve time resolution for operando studies. One application would be the study of novel battery materials with faster charge cycles. Alternatively, in addition to yielding the same resolution at shorter exposure times, the increase in coherent brightness would also enable higher resolutions at current exposure times for samples that can withstand the increased radiation dose. Radiation damage will become an issue for some samples. If the further increase in resolution is still desired, cryogenic cooling of the sample, enabled by specialized sample holders compatible with the sample stage in Nanosurveyor 2, will help to mitigate radiation damage.

Bibliography

[1] David Attwood and Anne Sakdinawat. *X-Rays and Extreme Ultraviolet Radiation*. Cambridge University Press, 2017.

[2] W. C. Röntgen. "On a New Kind of Rays". In: *Science* 3.59 (1896), pp. 227–231. ISSN: 00368075, 10959203.

[3] P Herrmann, K-A Steinhauser, R Gähler, Steyerl, A, and W Mampe. "Neutron microscope". In: *Physical review letters* 54.18 (1985), p. 1969.

[4] John Morgan, John Notte, Raymond Hill, and Bill Ward. "An introduction to the helium ion microscope". In: *Microscopy today* 14.4 (2006), pp. 24–31.

[5] Lord Rayleigh. "Wave theory of light". In: *Scientific Papers by John William Strutt, Baron Rayleigh* 3 (1902), pp. 47–189.

[6] Brent Fultz and James M. Howe. *Transmission Electron Microscopy and Diffractometry of Materials*. Springer, 2013.

[7] Roger Falcone, Chris Jacobsen, Janos Kirz, Stefano Marchesini, David Shapiro, and John Spence. "New directions in X-ray microscopy". In: *Contemporary Physics* 52.4 (2011), pp. 293–318.

[8] KV Kaznatcheev, Ch Karunakaran, UD Lanke, SG Urquhart, M Obst, and AP Hitchcock. "Soft X-ray spectromicroscopy beamline at the CLS: commissioning results". In: *Nuclear Instruments and Methods in Physics Research Section A: Accelerators, Spectrometers, Detectors and Associated Equipment* 582.1 (2007), pp. 96–99.

[9] Malcolm Howells, Christopher Jacobsen, Tony Warwick, and A Van den Bos. "Principles and applications of zone plate X-ray microscopes". In: *Science of microscopy*. Springer, 2007, pp. 835–926.

[10] D. A. Shapiro, Y-S Yu, T. Tyliszczak, J. Cabana, R. Celestre, W. Chao, K. Kaznatcheev, A. L. D. Kilcoyne, F. Maia, S. Marchesini, Y. Shirley Meng, T. Warwick, L. Lisheng Yang, and H. A. Padmore. "Chemical composition mapping with nanometre resolution by soft X-ray microscopy". In: *Nature Photonics* 8 (2014), pp. 765–769.

[11] Lord Rayleigh F.R.S. "XXXIV. On the transmission of light through an atmosphere containing small particles in suspension, and on the origin of the blue of the sky". In: *The London, Edinburgh, and Dublin Philosophical Magazine and Journal of Science* 47.287 (1899), pp. 375–384.

[12] KA Nugent, TE Gureyev, DF Cookson, D Paganin, and Z Barnea. "Quantitative phase imaging using hard x rays". In: *Physical review letters* 77.14 (1996), p. 2961.

[13] Marco Favaro, Beomgyun Jeong, Philip N Ross, Junko Yano, Zahid Hussain, Zhi Liu, and Ethan J Crumlin. "Unravelling the electrochemical double layer by direct probing of the solid/liquid interface". In: *Nature communications* 7 (2016), p. 12695.

[14] Stephanus Axnanda, Ethan J Crumlin, Baohua Mao, Sana Rani, Rui Chang, Patrik G Karlsson, Mårten OM Edwards, Måns Lundqvist, Robert Moberg, Phil Ross, et al. "Using 'tender' X-ray ambient pressure X-ray photoelectron spectroscopy as a direct probe of solid-liquid interface". In: *Scientific reports* 5 (2015), p. 9788.

[15] Michael F Lichterman, Shu Hu, Matthias H Richter, Ethan J Crumlin, Stephanus Axnanda, Marco Favaro, Walter Drisdell, Zahid Hussain, Thomas Mayer, Bruce S Brunschwig, et al. "Direct observation of the energetics at a semiconductor/liquid junction by operando X-ray photoelectron spectroscopy". In: *Energy & Environmental Science* 8.8 (2015), pp. 2409–2416.

[16] Anatoly Snigirev, Victor Kohn, Irina Snigireva, and Bruno Lengeler. "A compound refractive lens for focusing high-energy X-rays". In: *Nature* 384.6604 (1996), p. 49.

[17] Eugene Hecht. *Optics*. Addison-Wesley, 2002.

[18] L Kipp, M Skibowski, RL Johnson, R Berndt, R Adelung, S Harm, and R Seemann. "Sharper images by focusing soft X-rays with photon sieves". In: *Nature* 414.6860 (2001), p. 184.

[19] Donald H Bilderback. "Review of capillary x-ray optics from the 2nd International Capillary Optics Meeting". In: *X-Ray Spectrometry: An International Journal* 32.3 (2003), pp. 195–207.

[20] Chieh Chang and Anne Sakdinawat. "Ultra-high aspect ratio high-resolution nanofabrication for hard X-ray diffractive optics". In: *Nature communications* 5 (2014), p. 4243.

[21] MM O'Toole and AR Neureuther. "Influence of partial coherence on projection printing". In: *Developments in Semiconductor Microlithography IV*. Vol. 174. International Society for Optics and Photonics. 1979, pp. 22–28.

[22] Joseph W. Goodman. *Speckle phenomena in optics: theory and applications*. Roberts & Company, 2007.

[23] Dietbert Rudolph and Günter Schmahl. "High power zone plates for a soft X-ray microscope". In: *Annals of the New York Academy of Sciences* 342.1 (1980), pp. 94–104.

[24] H Rarback, D Shu, SC Feng, H Ade, J Kirz, I McNulty, DP Kern, THP Chang, Y Vladimirsky, N Iskander, et al. "Scanning x-ray microscope with 75-nm resolution". In: *Review of scientific instruments* 59.1 (1988), pp. 52–59.

[25] Janos Kirz, Chris Jacobsen, and Malcolm Howells. "Soft X-ray microscopes and their biological applications". In: *Quarterly reviews of biophysics* 28.1 (1995), pp. 33–130.

[26] Henry N Chapman, Chris Jacobsen, and Shawn Williams. "A characterisation of dark-field imaging of colloidal gold labels in a scanning transmission X-ray microscope". In: *Ultramicroscopy* 62.3 (1996), pp. 191–213.

[27] Konstantins Jefimovs, Joan Vila-Comamala, Marco Stampanoni, Burkhard Kaulich, and Christian David. "Beam-shaping condenser lenses for full-field transmission X-ray microscopy". In: *Journal of synchrotron radiation* 15.1 (2008), pp. 106–108.

[28] Dennis Gabor. "Microscopy by reconstructed wave-fronts". In: *Proceedings of the Royal Society of London. Series A. Mathematical and Physical Sciences* 197.1051 (1949), pp. 454–487.

[29] S Kikuta, S Aoki, S Kosaki, and K Kohra. "X-ray holography of lensless Fourier-transform type". In: *Optics Communications* 5.2 (1972), pp. 86–89.

[30] Sadao Aoki, Yutaka Ichihara, and Seishi Kikuta. "X-ray hologram obtained by using synchrotron radiation". In: *Japanese Journal of Applied Physics* 11.12 (1972), p. 1857.

[31] James E Trebes, Steven B Brown, E Michael Campbell, Dennis L Matthews, David G Nilson, Gary F Stone, and David A Whelan. "Demonstration of X-Ray holography with an X-Ray laser". In: *Science* 238.4826 (1987), pp. 517–519.

[32] M Howells, C Jacobsen, J Kirz, R Feder, K McQuaid, and S Rothman. "X-ray holograms at improved resolution: a study of zymogen granules". In: *Science* 238.4826 (1987), pp. 514–517.

[33] Miklós Tegze, Gy Faigel, Stefano Marchesini, M Belakhovsky, and AI Chumakov. "Three dimensional imaging of atoms with isotropic 0.5 Å resolution". In: *Physical review letters* 82.24 (1999), p. 4847.

[34] R W Gerchberg and W O Saxton. "A practical algorithm for the determination of phase from image and diffraction plane pictures". In: *Optik* 35 (1972), pp. 237–246.

[35] James R Fienup. "Reconstruction of an object from the modulus of its Fourier transform". In: *Optics letters* 3.1 (1978), pp. 27–29.

[36] R. H. T. Bates. "Fourier phase problems are uniquely soluble in more than one dimension. I: underlying theory". In: *Optik* 61 (1982), pp. 247–262.

[37] J. Miao, P. Charalambous, J. Kirz, and D. Sayre. "Extending the methodology of X-ray crystallography to allow imaging of micrometre-sized non-crystalline specimens". In: *Nature* 400 (1999), pp. 342–344.

[38] Veit Elser. "Phase retrieval by iterated projections". In: *JOSA A* 20.1 (2003), pp. 40–55.

[39] Stefano Marchesini, H He, Henry N Chapman, Stefan P Hau-Riege, Aleksandr Noy, Malcolm R Howells, Uwe Weierstall, and John CH Spence. "X-ray image reconstruction from a diffraction pattern alone". In: *Physical Review B* 68.14 (2003), p. 140101.

[40] Henry N Chapman, Anton Barty, Stefano Marchesini, Aleksandr Noy, Stefan P Hau-Riege, Congwu Cui, Malcolm R Howells, Rachel Rosen, Haifeng He, John CH Spence, et al. "High-resolution ab initio three-dimensional x-ray diffraction microscopy". In: *JOSA A* 23.5 (2006), pp. 1179–1200.

[41] Tomas Ekeberg, Martin Svenda, Chantal Abergel, Filipe RNC Maia, Virginie Seltzer, Jean-Michel Claverie, Max Hantke, Olof Jönsson, Carl Nettelblad, Gijs Van Der Schot, et al. "Three-dimensional reconstruction of the giant mimivirus particle with an x-ray free-electron laser". In: *Physical review letters* 114.9 (2015), p. 098102.

[42] Guoan Zheng, Roarke Horstmeyer, and Changhuei Yang. "Wide-field, high-resolution Fourier ptychographic microscopy". In: *Nature photonics* 7.9 (2013), p. 739.

[43] Kenneth A Goldberg, Markus P Benk, Antoine Wojdyla, David G Johnson, and Alexander P Donoghue. "New ways of looking at masks with the SHARP EUV microscope". In: *Extreme Ultraviolet (EUV) Lithography VI*. Vol. 9422. International Society for Optics and Photonics. 2015, 94221A.

[44] Antoine Wojdyla, Markus P Benk, Patrick P Naulleau, and Kenneth A Goldberg. "EUV photolithography mask inspection using Fourier ptychography". In: *Image Sensing Technologies: Materials, Devices, Systems, and Applications V*. Vol. 10656. International Society for Optics and Photonics. 2018, 106560W.

[45] Ian K Robinson, Ivan A Vartanyants, GJ Williams, MA Pfeifer, and JA Pitney. "Reconstruction of the shapes of gold nanocrystals using coherent x-ray diffraction". In: *Physical review letters* 87.19 (2001), p. 195505.

[46] Mark A Pfeifer, Garth J Williams, Ivan A Vartanyants, Ross Harder, and Ian K Robinson. "Three-dimensional mapping of a deformation field inside a nanocrystal". In: *Nature* 442.7098 (2006), p. 63.

[47] Brian Abbey, Keith A Nugent, Garth J Williams, Jesse N Clark, Andrew G Peele, Mark A Pfeifer, Martin De Jonge, and Ian McNulty. "Keyhole coherent diffractive imaging". In: *Nature Physics* 4.5 (2008), p. 394.

[48] Todd A Pitts and James F Greenleaf. "Fresnel transform phase retrieval from magnitude". In: *IEEE transactions on ultrasonics, ferroelectrics, and frequency control* 50.8 (2003), pp. 1035–1045.

[49] Henry N Chapman and Keith A Nugent. "Coherent lensless X-ray imaging". In: *Nature photonics* 4.12 (2010), p. 833.

[50] Stefano Marchesini and David Shapiro. *Coherent X-ray Diffraction Microscopy*. Wiley Online Library, 2008.

[51] Keith A Nugent. "Coherent methods in the X-ray sciences". In: *Advances in Physics* 59.1 (2010), pp. 1–99.

[52] Walter Hoppe. "Beugung im inhomogenen primärstrahlwellenfeld. i. prinzip einer phasenmessung von elektronenbeungungsinterferenzen". In: *Acta Crystallographica Section A: Crystal Physics, Diffraction, Theoretical and General Crystallography* 25.4 (1969), pp. 495–501.

[53] R Hegerl and W Hoppe. "Dynamic theory of crystalline structure analysis by electron diffraction in inhomogeneous primary wave field". In: *Berichte Der Bunsen-Gesellschaft Fur Physikalische Chemie* 74.11 (1970), p. 1148.

[54] Henry N Chapman. "Phase-retrieval X-ray microscopy by Wigner-distribution deconvolution". In: *Ultramicroscopy* 66.3-4 (1996), pp. 153–172.

[55] John M Rodenburg and Helen ML Faulkner. "A phase retrieval algorithm for shifting illumination". In: *Applied physics letters* 85.20 (2004), pp. 4795–4797.

[56] HML Faulkner and JM Rodenburg. "Movable aperture lensless transmission microscopy: a novel phase retrieval algorithm". In: *Physical review letters* 93.2 (2004), p. 023903.

[57] JM Rodenburg, AC Hurst, AG Cullis, BR Dobson, F Pfeiffer, O Bunk, C David, K Jefimovs, and I Johnson. "Hard-x-ray lensless imaging of extended objects". In: *Physical review letters* 98.3 (2007), p. 034801.

[58] Oliver Bunk, Martin Dierolf, Søren Kynde, Ian Johnson, Othmar Marti, and Franz Pfeiffer. "Influence of the overlap parameter on the convergence of the ptychographical iterative engine". In: *Ultramicroscopy* 108.5 (2008), pp. 481–487.

[59] Franz Pfeiffer. "X-ray ptychography". In: *Nature Photonics* 12.1 (2018), p. 9.

[60] John M Rodenburg. "Ptychography and related diffractive imaging methods". In: *Advances in imaging and electron physics* 150 (2008), pp. 87–184.

[61] Pierre Thibault, Martin Dierolf, Oliver Bunk, Andreas Menzel, and Franz Pfeiffer. "Probe retrieval in ptychographic coherent diffractive imaging". In: *Ultramicroscopy* 109.4 (2009), pp. 338–343.

[62] Pierre Thibault, Martin Dierolf, Andreas Menzel, Oliver Bunk, Christian David, and Franz Pfeiffer. "High-resolution scanning x-ray diffraction microscopy". In: *Science* 321.5887 (2008), pp. 379–382.

[63] Andreas Schropp, Robert Hoppe, Vivienne Meier, Jens Patommel, Frank Seiboth, Hae Ja Lee, Bob Nagler, Eric C Galtier, Brice Arnold, Ulf Zastrau, et al. "Full spatial characterization of a nanofocused x-ray free-electron laser beam by ptychographic imaging". In: *Scientific reports* 3 (2013), p. 1633.

[64] Cameron M Kewish, Pierre Thibault, Martin Dierolf, Oliver Bunk, Andreas Menzel, Joan Vila-Comamala, Konstantins Jefimovs, and Franz Pfeiffer. "Ptychographic characterization of the wavefield in the focus of reflective hard X-ray optics". In: *Ultramicroscopy* 110.4 (2010), pp. 325–329.

[65] Andrew M Maiden and John M Rodenburg. "An improved ptychographical phase retrieval algorithm for diffractive imaging". In: *Ultramicroscopy* 109.10 (2009), pp. 1256–1262.

[66] Pierre Thibault and Andreas Menzel. "Reconstructing state mixtures from diffraction measurements". In: *Nature* 494.7435 (2013), p. 68.

[67] B Enders, M Dierolf, P Cloetens, M Stockmar, F Pfeiffer, and P Thibault. "Ptychography with broad-bandwidth radiation". In: *Applied Physics Letters* 104.17 (2014), p. 171104.

[68] Huibin Chang, Pablo Enfedaque, Yifei Lou, and Stefano Marchesini. "Partially coherent ptychography by gradient decomposition of the probe". In: *Acta Crystallographica Section A: Foundations and Advances* 74.3 (2018), pp. 157–169.

[69] B Enders and P Thibault. "A computational framework for ptychographic reconstructions". In: *Proceedings of the Royal Society A: Mathematical, Physical and Engineering Sciences* 472.2196 (2016), p. 20160640.

[70] Mike Beckers, Tobias Senkbeil, Thomas Gorniak, Klaus Giewekemeyer, Tim Salditt, and Axel Rosenhahn. "Drift correction in ptychographic diffractive imaging". In: *Ultramicroscopy* 126 (2013), pp. 44–47.

[71] Fucai Zhang, Isaac Peterson, Joan Vila-Comamala, Ana Diaz, Felisa Berenguer, Richard Bean, Bo Chen, Andreas Menzel, Ian K Robinson, and John M Rodenburg. "Translation position determination in ptychographic coherent diffraction imaging". In: *Optics express* 21.11 (2013), pp. 13592–13606.

[72] AM Maiden, MJ Humphry, MC Sarahan, B Kraus, and JM Rodenburg. "An annealing algorithm to correct positioning errors in ptychography". In: *Ultramicroscopy* 120 (2012), pp. 64–72.

[73] Stefano Marchesini, Hari Krishnan, Benedikt J Daurer, David A Shapiro, Talita Perciano, James A Sethian, and Filipe RNC Maia. "SHARP: a distributed GPU-based ptychographic solver". In: *Journal of applied crystallography* 49.4 (2016), pp. 1245–1252.

[74] P Thibault and M Guizar-Sicairos. "Maximum-likelihood refinement for coherent diffractive imaging". In: *New Journal of Physics* 14.6 (2012), p. 063004.

[75] Ondrej Mandula, Marta Elzo Aizarna, Joël Eymery, Manfred Burghammer, and Vincent Favre-Nicolin. "PyNX. Ptycho: a computing library for X-ray coherent diffraction imaging of nanostructures". In: *Journal of Applied Crystallography* 49.5 (2016), pp. 1842–1848.

[76] Youssef SG Nashed, David J Vine, Tom Peterka, Junjing Deng, Rob Ross, and Chris Jacobsen. "Parallel ptychographic reconstruction". In: *Optics express* 22.26 (2014), pp. 32082–32097.

[77] M Holler, A Diaz, M Guizar-Sicairos, P Karvinen, Elina Färm, Emma Härkönen, Mikko Ritala, A Menzel, J Raabe, and O Bunk. "X-ray ptychographic computed tomography at 16 nm isotropic 3D resolution". In: *Scientific reports* 4 (2014), p. 3857.

[78] Young-Sang Yu, Maryam Farmand, Chunjoong Kim, Yijin Liu, Clare P Grey, Fiona C Strobridge, Tolek Tyliszczak, Rich Celestre, Peter Denes, John Joseph, et al. "Three-dimensional localization of nanoscale battery reactions using soft X-ray tomography". In: *Nature communications* 9.1 (2018), p. 921.

[79] Doğa Gürsoy. "Direct coupling of tomography and ptychography". In: *Optics letters* 42.16 (2017), pp. 3169–3172.

[80] Selin Aslan, Viktor Nikitin, Daniel J Ching, Tekin Bicer, Sven Leyffer, and Doğa Gürsoy. "Joint ptycho-tomography reconstruction through alternating direction method of multipliers". In: *Optics Express* 27.6 (2019), pp. 9128–9143.

[81] David Shapiro, Pierre Thibault, Tobias Beetz, Veit Elser, Malcolm Howells, Chris Jacobsen, Janos Kirz, Enju Lima, Huijie Miao, Aaron M Neiman, et al. "Biological imaging by soft x-ray diffraction microscopy". In: *Proceedings of the National Academy of Sciences* 102.43 (2005), pp. 15343–15346.

[82] David A Shapiro, Rich Celestre, Peter Denes, Maryam Farmand, John Joseph, ALD Kilcoyne, Stefano Marchesini, Howard Padmore, Singanallur V Venkatakrishnan, Tony Warwick, et al. "Ptychographic imaging of nano-materials at the advanced light source with the nanosurveyor instrument". In: *Journal of Physics: Conference Series*. Vol. 849. 1. IOP Publishing. 2017, p. 012028.

[83] David Shapiro, S Roy, R Celestre, W Chao, D Doering, M Howells, S Kevan, D Kilcoyne, J Kirz, S Marchesini, et al. "Development of coherent scattering and diffractive imaging and the COSMIC facility at the Advanced Light Source". In: *Journal of Physics: Conference Series*. Vol. 425. 19. IOP Publishing. 2013, p. 192011.

[84] Andreas Karl Schmid and Nord Andresen. *Motorized manipulator for positioning a TEM specimen*. US Patent 7,851,769. Dec. 2010.

[85] Peter Ercius, Markus Boese, Thomas Duden, and Ulrich Dahmen. "Operation of TEAM I in a user environment at NCEM". In: *Microscopy and Microanalysis* 18.4 (2012), pp. 676–683.

[86] P Denes, D Doering, HA Padmore, J-P Walder, and J Weizeorick. "A fast, direct x-ray detection charge-coupled device". In: *Review of Scientific Instruments* 80.8 (2009), p. 083302.

[87] Richard Celestre, Kasra Nowrouzi, David A Shapiro, Peter Denes, John M Joseph, Andreas Schmid, and Howard A Padmore. "Nanosurveyor 2: A Compact Instrument for Nano-Tomography at the Advanced Light Source". In: *Journal of Physics: Conference Series*. Vol. 849. 1. IOP Publishing. 2017, p. 012047.

[88] Valeriy V Yashchuk, Wayne R McKinney, and Peter Z Takacs. "Binary pseudorandom grating standard for calibration of surface profilometers". In: *Optical Engineering* 47.7 (2008), p. 073602.

[89] S Babin, N Bouet, S Cabrini, G Calafiore, R Conley, G Gevorkyan, K Munechika, A Vladár, and VV Yashchuk. "1.5 nm fabrication of test patterns for characterization of metrological systems". In: *Metrology, Inspection, and Process Control for Microlithography XXXI*. Vol. 10145. International Society for Optics and Photonics. 2017, p. 1014518.

[90] VV Yashchuk, PJ Fischer, ER Chan, R Conley, WR McKinney, NA Artemiev, N Bouet, S Cabrini, G Calafiore, I Lacey, et al. "Binary pseudo-random patterned structures for modulation transfer function calibration and resolution characterization of a full-field transmission soft x-ray microscope". In: *Review of Scientific Instruments* 86.12 (2015), p. 123702.

[91] Jinghua Guo. "Soft x-ray absorption and emission spectroscopy in the studies of nanomaterials". In: *X-Rays in Nanoscience: Spectroscopy, Spectromicroscopy, and Scattering Techniques, edited by J. Guo (Wiley-VCH Verlag GmbH & Co. KGaA, Weinheim, Germany, 2010)* (2010).

[92] Adam P Hitchcock. "Soft X-ray spectromicroscopy and ptychography". In: *Journal of Electron Spectroscopy and Related Phenomena* 200 (2015), pp. 49–63.

[93] M Lerotic, C Jacobsen, T Schäfer, and S Vogt. "Cluster analysis of soft X-ray spectromicroscopy data". In: *Ultramicroscopy* 100.1-2 (2004), pp. 35–57.

[94] Naoki Nitta, Feixiang Wu, Jung Tae Lee, and Gleb Yushin. "Li-ion battery materials: present and future". In: *Materials today* 18.5 (2015), pp. 252–264.

[95] A Thompson, D Attwood, E Gullikson, M Howells, J Kortright, A Robinson, et al. "X-ray data booklet (2009)". In: *URL http://xdb. lbl. gov* (2009).

[96] Antonio Visioli. *Practical PID control*. Springer Science & Business Media, 2006.

[97] Michael A Johnson and Mohammad H Moradi. *PID control*. Springer, 2005.

[98] Manuel Guizar-Sicairos, Mirko Holler, Ana Diaz, Joan Vila-Comamala, Oliver Bunk, and Andreas Menzel. "Role of the illumination spatial-frequency spectrum for ptychography". In: *Physical Review B* 86.10 (2012), p. 100103.

[99] Xiaojing Huang, Hanfei Yan, Ross Harder, Yeukuang Hwu, Ian K Robinson, and Yong S Chu. "Optimization of overlap uniformness for ptychography". In: *Optics Express* 22.10 (2014), pp. 12634–12644.

[100] Mikael Eriksson, J Friso van der Veen, and Christoph Quitmann. "Diffraction-limited storage rings–a window to the science of tomorrow". In: *Journal of synchrotron radiation* 21.5 (2014), pp. 837–842.

[101] Stefano Marchesini and Anne Sakdinawat. "Shaping coherent x-rays with binary optics". In: *Optics express* 27.2 (2019), pp. 907–917.